

Adaptive variational low-rank dynamics for open quantum systems

Luca Gravina ^{1,2,*} and Vincenzo Savona ^{1,2,†}¹*Institute of Physics, Ecole Polytechnique Fédérale de Lausanne (EPFL), CH-1015 Lausanne, Switzerland*²*Center for Quantum Science and Engineering, Ecole Polytechnique Fédérale de Lausanne (EPFL), CH-1015 Lausanne, Switzerland*

(Received 12 January 2024; accepted 29 March 2024; published 19 April 2024)

We introduce a model-independent method for the efficient simulation of low-entropy systems, whose dynamics can be accurately described with a limited number of states. Our method leverages the time-dependent variational principle to efficiently integrate the Lindblad master equation, dynamically identifying and modifying the low-rank basis over which we decompose the system's evolution. By dynamically adapting the dimension of this basis, and thus the rank of the density matrix, our method maintains optimal representation of the system state, offering a substantial computational advantage over existing adaptive low-rank schemes in terms of both computational time and memory requirements. We demonstrate the efficacy of our method through extensive benchmarks on a variety of model systems, with a particular emphasis on multiqubit bosonic codes, a promising candidate for fault-tolerant quantum hardware. Our results highlight the method's versatility and efficiency, making it applicable to a wide range of systems characterized by arbitrary degrees of entanglement and moderate entropy throughout their dynamics. We provide an implementation of the method as a Julia package, making it readily available to use.

DOI: [10.1103/PhysRevResearch.6.023072](https://doi.org/10.1103/PhysRevResearch.6.023072)

I. INTRODUCTION

In the path towards scalable and reliable quantum hardware [1–8], the loss of quantum coherence due to interactions with an external environment presents a crucial limitation. While environmental interactions are often known for introducing noise and hindering quantum effects, under careful control, they can also serve as a resource, often harbouring surprising benefits not found in equilibrium systems. These features have long been exploited for various applications, including the preparation and stabilization of quantum states [9–11], protocols for quantum error correction and suppression [5,12–20], enhancement of metrological protocols [21–23], and the stabilization and control of entangled, topological, and localized phases [24–28].

Understanding the impact of both incoherent and coherent relaxation processes on quantum systems is therefore crucial for the progress of quantum technologies. Consequently, the development of fast and scalable methods for their classical simulation is equally important. The exact numerical simulation of many-body quantum systems, however, suffers from the curse of dimensionality, namely the exponential growth of computational resources, scaling as d^N , required to simulate the dynamics of a system with N identical modes, each

with d possible states. As a result, simulating even moderately large quantum systems becomes rapidly an intractable problem [29].

When a system is not isolated, but couples to the degrees of freedom of an external environment, the two become entangled. The system's state is then represented by a Hermitian positive semidefinite operator, the density matrix, resulting from tracing out the environmental degrees of freedom. Under the assumption of a memoryless environment, the time evolution of the density matrix is governed by the Lindblad master equation [30–32] which has found application in a very broad range of physical settings [33]. In this context, the curse of dimensionality becomes even more daunting, with computational requirements scaling as d^{2N} . Different approaches for mitigating the complexity of the task exist [34], each one compromising on the degree of accuracy with which different features of the statistical ensemble can be captured. Among these, Monte Carlo quantum trajectory methods [35,36], phase-space methods [37,38], semiclassical approximations [39,40], tensor network techniques [34,41–47], and variational approaches [48–55] possibly coupled with Monte Carlo sampling and neural network techniques [56–62], stand out.

In recent years, another class of methods known as *ensemble truncation methods* has emerged as a powerful tool for simulating isolated [63–67] and dissipative quantum systems [68–71]. This approach is based on the realization that many quantum systems, particularly those with low entropy, can be effectively represented by a density matrix of significantly lower rank than what the whole Hilbert space would require. This reduction is achieved by focusing on a subset of states that capture the essential structure of the statistical ensemble characterizing the mixed quantum state, thereby reducing

*luca.gravina@epfl.ch

†vincenzo.savona@epfl.ch

computational complexity while maintaining accuracy. The low-rank (LR) hypothesis applies to many systems of physical interest. Among these are systems weakly coupled to the environment or systems initialized in a pure, i.e., zero-entropy state, in the early stage of their dynamics. Modern quantum-computing platforms, designed to minimize dissipation and noise, often fall in either of the above instances.

A considerable challenge remains, however, determining how the LR states should evolve to optimally represent the density matrix along the time evolution and in particular how the dimension of the LR subspace should vary to accommodate changes of the entropy over time. Building on this premise, this paper introduces a method encapsulating the most relevant features of the ensemble truncation schemes within the robust framework of the time-dependent variational principle (TDVP) developed for open quantum systems in Refs. [48,72–74]. Indeed, our method, which we deem the *LR-TDVP method*, effectively integrates the benefits of both approaches. On the one side, it leverages the dynamical truncation method’s ability to efficiently represent quantum states with minimal information loss while dynamically adjusting the dimension of the variational basis to adapt to changes in the system’s entropy. On the other, it takes advantage of the variational principle to dynamically modify the LR basis to ensure the optimal fidelity of the evolution.

A remark is in order. The reduced number of states that LR methods use to approximate the statistical mixture limits the amount of mixedness or entropy we can efficiently account for. On the other hand, taking an exact representation of the variational states allows us to describe arbitrarily entangled or correlated states entering the statistical mixture. In this respect, LR methods are the natural complement of techniques based on, e.g., tensor-network representations [75–79], which are inherently limited in the amount of quantum correlations they can encode but can represent arbitrary amounts of mixedness.

This combination of constraints is often satisfied by modern quantum hardware. By addressing the challenges faced in the NISQ era, our method offers a significant advancement in the simulation of complex quantum systems, paving the way for new discoveries and applications in quantum computing and simulation.

Our method is designed to be universally applicable, independent of specific system characteristics such as spatial symmetries, particle statistics, geometry of the space, or topology of the interactions. To facilitate its use and integration into various research workflows, we have incorporated into the QuantumToolbox library [80], a Julia-based [81] quantum physics toolkit. The library, along with our method, is readily accessible and examples showcasing its use for the creation of some of the figures of the paper can be found at the repository listed in Ref. [82].

II. THE LOW-RANK TDVP

Let us consider an open quantum system whose dynamics is described by the Lindblad master equation,

$$\frac{\partial \hat{\rho}}{\partial t} = \mathcal{L}(\hat{\rho}) = -i[\hat{H}, \hat{\rho}] + \sum_{\sigma=1}^D \mathcal{D}[\hat{\Gamma}_{\sigma}] \hat{\rho}, \quad (1)$$

where $\hat{\rho} \equiv \rho(t)$ (for brevity) is the system density matrix at time t , \mathcal{L} is the Liouvillian superoperator, and we take $\hbar = 1$. While the coherent part of the dynamics is described by the Hamiltonian \hat{H} acting on a Hilbert space \mathcal{H} of dimension $N_{\mathcal{H}}$, the incoherent evolution is described by the dissipator,

$$D[\hat{\Gamma}] \hat{\rho} = \hat{\Gamma} \hat{\rho} \hat{\Gamma}^{\dagger} - \frac{1}{2} \{ \hat{\Gamma}^{\dagger} \hat{\Gamma}, \hat{\rho} \}, \quad (2)$$

which formalizes the action of the jump operator $\hat{\Gamma}$ on the system.

The exact numerical simulation of this dynamics is generally computationally challenging due to the exponential scaling of the required resources, growing as the square of the Hilbert space dimension. The focus of our work is, however, on low-entropy systems, whose dynamics is known to be well captured, at all times, by a limited number of states $\{|\varphi_k(t)\rangle; k = 1, \dots, M\}$ with $M \ll N_{\mathcal{H}}$. These states span the *low-rank* subspace $\mathcal{H}_M \subseteq \mathcal{H}$ which is assumed to encapsulate the essential structure of the statistical ensemble throughout the dynamics. In recent years, various heuristic algorithms have been developed that effectively truncate the density matrix $\hat{\rho}$ to a rank- M matrix, significantly smaller than what the whole Hilbert space would require. Such methods are collectively known as *ensemble truncation methods* [68–71]. Fundamental to these methods is their ability to dynamically adjust the truncation rank $M = M(t)$ at each time step, adapting to an entropy landscape that varies over time. However, a rigorous and systematic approach for selecting and adapting the low-rank basis states remains a challenge.

Concurrently, *variational methods* have emerged as a versatile tool for circumventing the exponential space problem by considering trial states from a physically motivated, small subset of the exponentially large Hilbert space [48]. In these methods, the density matrix $\hat{\rho}(t) = \hat{\rho}[\theta(t)]$ is expressed in terms of a set of variational parameters $\theta(t)$ which evolve in time to guarantee, within the expressiveness of the ansatz, the optimal approximation of the evolution generated by the action of \mathcal{L} on $\hat{\rho}(t)$.

In this work, we introduce the low-rank TDVP algorithm where the benefits of both classes of methods are united. By employing the McLachlan TDVP we rigorously estimate the optimal subspace $\mathcal{H}_{M(t)}$ over which to decompose the evolution at each time step (Sec. II A). Additionally, we develop schemes to dynamically adjust the dimension of this subspace in response to changes in the system’s entropy (Sec. II B). Defering a detailed analysis of the ensemble truncation methods to Appendix C, we last compare our variational method to the heuristic algorithms established in Refs. [68–70] (Sec. II C). The main features of this method are summarized in Fig. 1.

A. Variational equations of motion

The most general variational parametrization of an arbitrary statistical ensemble can be expressed as:

$$\hat{\rho}(t) = \sum_{i,j=1}^{M(t)} B_{ij}(t) |\varphi_i(t)\rangle \langle \varphi_j(t)|, \quad (3)$$

with $B_{ij}(t)$ being time dependent, Hermitian coefficients [$B_{ij}(t) = B_{ji}(t)^*$]. This formulation confines the dynamics to the variational manifold spanned by the states $\{|\varphi_k(t)\rangle\}$;

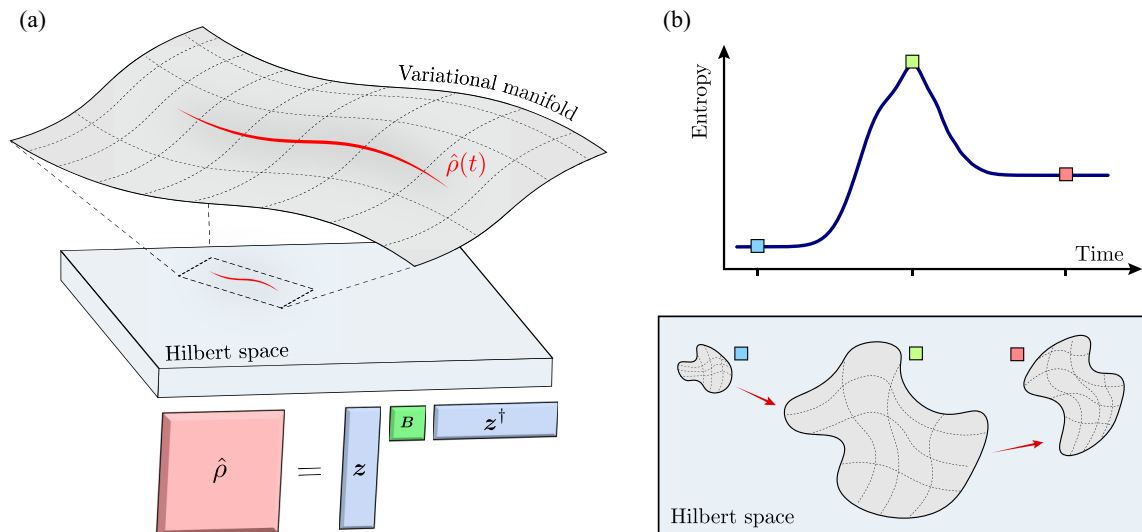


FIG. 1. Illustrative overview of the LR-TDVP method. (a) Top: Pictorial representation of the density matrix $\rho(t)$ (depicted in red) at a generic time t during the dynamics. The variational manifold selectively encompasses a specific region of the Hilbert space, capturing the predominant components of the statistical ensemble at time t . Bottom: Illustration of how memory efficiency is achieved by decomposing the $N_{\mathcal{H}} \times N_{\mathcal{H}}$ density matrix into smaller $N_{\mathcal{H}} \times M$ and $M \times M$ matrices. (b) Schematic representation of the dynamic adjustment of the variational manifold's dimension. Both the manifold and the rank of the truncated density matrix are dynamically modified to maintain a consistent level of accuracy, adapting to changes in the system's entropy. This adjustment reflects the principle that highly entropic systems necessitate a larger number of states for accurate representation, whereas low-entropy ensembles can be effectively described with fewer states.

$k = 1, \dots, M(t)$ whose number we adapt in time to accommodate changes in the system's entropy. Throughout the paper we will refer to $|\varphi_k(t)\rangle$ as the *variational* or *low-rank states* and to $M(t)$ as the *rank* of $\hat{\rho}$.

Importantly, the variational method ensures a dynamical adjustment of the variational states, guaranteeing the optimal set of states is selected at all times to best approximate the evolution under \mathcal{L} . To enable this dynamic adjustment, the variational states themselves must be parametrized. In our approach, we adopt a full linear parametrization, decomposing $|\varphi_k\rangle$ on the computational basis $\{|e_\alpha\rangle\}_{\alpha=1, \dots, N_{\mathcal{H}}}$ as

$$|\varphi_k(t)\rangle = \sum_{\alpha=1}^{N_{\mathcal{H}}} z_{\alpha,k}(t) |e_\alpha\rangle. \quad (4)$$

For clarity, and where this does not lead to confusion, we will omit the time argument in subsequent discussions. While the present work focuses on a full linear parametrization of the variational states, alternative parametrizations relying on tensor networks or neural network architectures are indeed possible and will be subject of future investigation.

The dynamical problem outlined in Eq. (1) can now be reformulated into a set of equations of motion (EOM) for the variational parameters, comprising the population matrix $\mathbf{B} = [B_{ij}]$ and the coefficient matrix $\mathbf{z} = [z_{\alpha k}]$. To derive these EOM, we apply the McLachlan variational principle, with the additional constraint of trace preservation:

$$\delta \left[\left\| \left(\frac{d}{dt} - \mathcal{L} \right) \hat{\rho} \right\|^2 + \lambda \frac{d}{dt} \text{Tr}\{\hat{\rho} + \hat{\rho}^\dagger\} \right] = 0. \quad (5)$$

Note that in this notation, the time derivative of the density matrix $\dot{\hat{\rho}} = d\hat{\rho}/dt$ is intended with respect to the

variational parameters, i.e., $\dot{\hat{\rho}} = \nabla_{\theta} \hat{\rho}(\theta) \cdot \dot{\theta}$. Here λ is the Lagrange multiplier associated to the trace-preservation constraint $d\text{Tr}\{\hat{\rho} + \hat{\rho}^\dagger\}/dt = 0$. This constraint was chosen, over the more obvious choice $d\text{Tr}\{\hat{\rho}\}/dt = 0$, to preserve symmetry under complex conjugation. The norm $\|\hat{c}\| \equiv \text{Tr}\{\hat{c}^\dagger \hat{c}\}$ is the Frobenius or Hilbert-Schmidt norm.

While Eq. (5) is general in scope, substituting Eq. (3) for $\hat{\rho}$ yields the EOM specific for the chosen ansatz (details on the derivation are provided in Appendix A):

$$\begin{aligned} \dot{\mathbf{B}} &= \left(\mathbf{S}^{-1} \mathbf{L} - \frac{\text{Tr}\{\mathbf{S}^{-1} \mathbf{L}\}}{M} \mathbf{1} \right) \mathbf{S}^{-1} \\ \dot{\mathbf{z}} &= (\tilde{\mathbf{L}} - \mathbf{z} \mathbf{S}^{-1} \mathbf{L}) \mathbf{S}^{-1} \mathbf{B}^{-1}, \end{aligned} \quad (6)$$

where $\tilde{\mathbf{L}} = \mathcal{L}(\hat{\rho})\mathbf{z}$, $\mathbf{L} = \mathbf{z}^\dagger \tilde{\mathbf{L}}$, $\mathbf{S} = \mathbf{z}^\dagger \mathbf{z}$, while \mathbf{S}^{-1} and \mathbf{B}^{-1} denote the inverse matrices of \mathbf{S} and \mathbf{B} , respectively. Since both \mathbf{S} and \mathbf{B} may be singular, their inverse is often ill defined. To overcome this problem, throughout the paper we adopt a smooth regularization criterion based on the singular value decomposition of the two matrices, as proposed in Ref. [83] (details in Appendix B).

The dynamics of the system can now be obtained by numerical integration of Eq. (6) which we perform using high-order adaptive-time-step solvers. Each time step requires the calculation of \mathbf{B}^{-1} and of $\tilde{\mathbf{L}}$. The first we perform using singular value decomposition, while the second only requires matrix multiplications, the most extensive being between (extremely sparse) $N_{\mathcal{H}} \times N_{\mathcal{H}}$ and (dense) $N_{\mathcal{H}} \times M$ matrices. Notably, since for a linear parametrization $\dot{\mathbf{S}} = 0$ (see Appendix A), the computation of \mathbf{S}^{-1} incurs no additional computational cost after its initial calculation at the beginning of the process.

As previously anticipated, within each integration step, if $M \ll N_{\mathcal{H}}$ (LR hypothesis), then both the speed and storage requirements for the calculation are dramatically improved. For additional information on the computational costs and procedures, we refer readers to Appendix B.

B. Dynamical rank update

A critical aspect of any LR approach is its capability to dynamically adjust the dimension of the LR basis throughout the system's evolution [$M = M(t)$]. This adaptability is essential for accommodating changes in the system's entropy over time. In the ensemble truncation methods [68–70], this update is achieved by truncating the full-rank density matrix $\hat{\rho}(t + dt)$ at each time step with the goal of keeping a control quantity, namely the truncation error $\epsilon_M = 1 - \sum_{j=1}^M p_j$, below a predefined threshold ϵ_{\max} . In this section we detail schemes for efficiently implementing a dynamic update of the dimension of the variational basis in our approach.

1. Basis inflation

Let us first consider the basis inflation problem, where the system's entropy increases over time. An example of a system presenting this behavior is developed in Sec. III A. To start, we posit the existence of a control quantity $\chi(t)$ that accurately reflects the solution's accuracy and that can be efficiently computed at each time step. Various options for χ will be discussed below. This quantity is monitored through a callback mechanism, continuously evaluated against a predefined upper bound of ϵ_{\max} . Initially zero at $t = 0$, χ grows with the system's entropy and, hence, over time. Let t^* denote the time when $\chi(t^*) = \epsilon_{\max}$. At this time, the rank is incrementally increased from M to $M + 1$ through the addition of a new state $|\varphi_{M+1}\rangle$ to the LR basis. The population and coherences associated with this new state are initially vanishing [$B_{j,M+1} = (B_{M+1,j})^* = 0$] to ensure continuity in the solution. The variational principle ensures that the solution can be made independent of the specific choice of $|\varphi_{M+1}\rangle$. This independence, within the specified tolerance, is guaranteed if the state is added at a time prior to t^* , ensuring that $|\varphi_{M+1}\rangle(t^*)$ satisfies the TDVP at that time. To achieve this, we implement periodic checkpoints at intervals of Δt . Each time a threshold crossing is registered, the integration is restarted with an enlarged basis from the nearest checkpoint before the crossing. This approach also ensures that the bound on χ remains strict, as the response in χ may not be immediate following the basis inflation. However, we observe that in most situations of interest, an instantaneous basis inflation ($\Delta t = 0$) does not significantly compromise the solution's accuracy, suggesting that the variational adjustment of $|\varphi_{M+1}\rangle$ is almost instantaneous. This is illustrated in Fig. 2, where we display $\chi(t)$ for both $\Delta t = 0$ and $\Delta t = 0.2$. As shown in the inset, the trace-distance

$$D(\hat{A}, \hat{B}) = \frac{1}{2} \text{Tr} \left\{ \sqrt{(\hat{A} - \hat{B})^\dagger (\hat{A} - \hat{B})} \right\}, \quad (7)$$

evaluated between the exact and approximated solutions remains virtually unchanged when choosing $\Delta t = 0$.

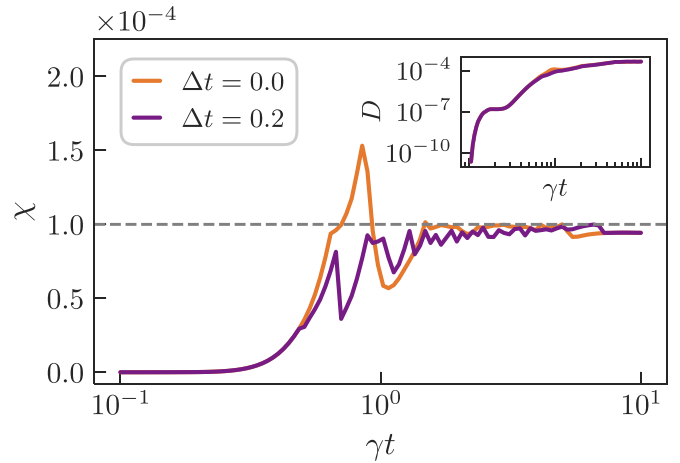


FIG. 2. Time evolution of the approximate variational error, $\chi(t)$, as defined in Eq. (10). The upper bound for χ is set at $\epsilon_{\max} = 10^{-4}$, which strictly applies for $\Delta t > 0$. The inset displays the distance between the true solution and the truncated one as obtained from Eq. (7). The physical model underlying this example is the XYZ Heisenberg model (detailed in Sec. III A) with $N = 9$ spins and $J_y = 1$. The values of all remaining physical parameters [see Eqs. (11) and (12)] are the same as those used in Fig. 4.

2. Basis deflation

For the basis deflation problem, we adopt a similar approach to that used for basis inflation. Consider a case where the system's entropy, after peaking, gradually diminishes as the system approaches the stationary state. An example of such dynamics is discussed in Sec. III C. In this context, to enhance efficiency, it is desirable to reduce the dimension of $\hat{H}_{M(t)}$ when χ falls below a lower threshold ϵ_{\min} . Upon crossing this threshold, the rank is incrementally decreased from M to $M - 1$ by removing a state from the LR basis. A proper selection of which state to remove from the basis is critical for the success of the deflation protocol. Intuitively, we should eliminate the state contributing the least to the dynamics, potentially the one with the lowest occupancy. This approach has two primary limitations. First, it is basis dependent; small diagonal elements in one basis may not be so small in another, potentially leading us to overlook an optimal lower rank basis. Second, eliminating the state with the lowest occupancy also removes all correlations between the selected state and other states with larger occupancy, impacting the accuracy of the solution. Although the magnitude of such correlations is constrained by the positivity and trace constraints on $\hat{\rho}$ (i.e., $|\rho_{ij}| \leq \sqrt{\rho_{ii}} \sqrt{\rho_{jj}}$), the resultant errors, albeit small, may accumulate over time.

To mitigate these issues, we first transition to the diagonal basis by diagonalizing $\hat{\rho}(t)$ as

$$\hat{\rho}(t) = \sum_{j=1}^M p_j |\eta_j\rangle\langle\eta_j|, \quad (8)$$

with $p_1 \geq p_2 \geq \dots \geq p_M$. Subsequently, we remove the M th state from the basis but maintain the equivalent diagonal representation of the LR basis, resulting in $\mathbf{z}(t + dt) = (|\eta_1\rangle, \dots, |\eta_{M-1}\rangle)$ and $\mathbf{B}(t + dt) = \text{diag}(p_1, \dots, p_{M-1})$.

Importantly, the Schur-Horn theorem [84] assures that the smallest diagonal element of $\hat{\rho}(t)$ in any basis will exceed its smallest eigenvalue, effectively resolving the first limitation. Moreover, transitioning to a diagonal basis allows for the inclusion of previously neglected correlations into the new variational states, thereby overcoming the second limitation.

Efficient diagonalization of $\hat{\rho}(t)$ is feasible by recognizing that $\hat{\rho}(t)$ can be expressed as $\hat{\rho} = \hat{C}\hat{C}^\dagger$, where $\hat{C} = \mathbf{z}\sqrt{\mathbf{B}}$. As discussed in Refs. [68–70], this matrix shares the same nonvanishing eigenvalues p_j as the small $M \times M$ matrix $\hat{\sigma} = \hat{C}^\dagger\hat{C}$. The eigenvectors of these two matrices are related through \hat{C} . It is important to note that, unlike the basis inflation case, failing to reduce the rank in the deflation scenario does not lead to a less-accurate solution. Quite the contrary, the solution will be more accurate, albeit at a higher computational cost.

3. Control quantities

We now provide a set of possible choices for χ . Given the variational parametrization of the LR states, the natural control quantity for our method is the distance between the true evolution and the variational evolution of the trial state, calculated as [48]

$$\chi = \|\dot{\hat{\rho}} - \mathcal{L}(\hat{\rho})\|. \quad (9)$$

We recall once more that in this notation $\dot{\hat{\rho}} = \nabla_{\theta}\hat{\rho}(\theta) \cdot \dot{\theta}$ where $\theta = (\mathbf{z}, \mathbf{B})$ (see Appendix A for details). The only linear algebra operations involved in the computation of Eq. (9) are matrix multiplications, the largest of which between extremely sparse $N_{\mathcal{H}} \times N_{\mathcal{H}}$ matrices and dense $N_{\mathcal{H}} \times M$ matrices. The number of matrix multiplications to be computed scales as D^2 , the square of the number of jump operators.

A more efficient choice, which comes at no additional computational cost, is

$$\chi = \text{Tr}\{\mathbf{S}^{-1}\mathbf{L}\} = \text{Tr}\{\mathbf{P}\mathcal{L}(\hat{\rho})\}, \quad (10)$$

where $\mathbf{P} = \mathbf{z}\mathbf{S}^{-1}\mathbf{z}^\dagger$ is the projector on the LR manifold. We adopted this choice for all simulations in the paper. Although $\text{Tr}\{\mathcal{L}(\hat{\rho})\} = 0$ for any physical density matrix $\hat{\rho}$ and Liouvillian \mathcal{L} , $\text{Tr}\{\mathbf{P}\mathcal{L}(\hat{\rho})\}$ can be nonzero as a result of projecting over an incomplete basis [74,85]. Indeed, $\text{Tr}\{\mathbf{P}\mathcal{L}(\hat{\rho})\}$ is only vanishing when $\hat{\rho}$ is entirely contained in the LR manifold. Assuming the latter to be constructed around the initial state of the simulation, $\text{Tr}\{\mathbf{P}\mathcal{L}(\hat{\rho})\}$ vanishes at $t = 0$, and in an ideal evolution would remain so throughout the dynamics. Its departure from zero quantifies leakage outside of the variational manifold, and as such, it is a good indicator of the solution's accuracy in real time. This choice for χ is closely related to the truncation error ϵ_M of Ref. [68], as can be seen from the perturbative expansion carried out in Appendix C.

The last criterion we propose takes $\chi = p_M/p_1$ where the probabilities p_i follow from the diagonalization of $\hat{\rho}(t)$ according to Eq. (8).

Figure 3 confirms that all three choices of χ proposed above are well-suited control parameters. Here we display, as a function of the error threshold ϵ_{\max} , the rank M of the approximated steady-state solution and the associated trace-distance from the full simulation [cf. Eq. (7)]. As expected, the rank M of the approximate solution increases the lower we set

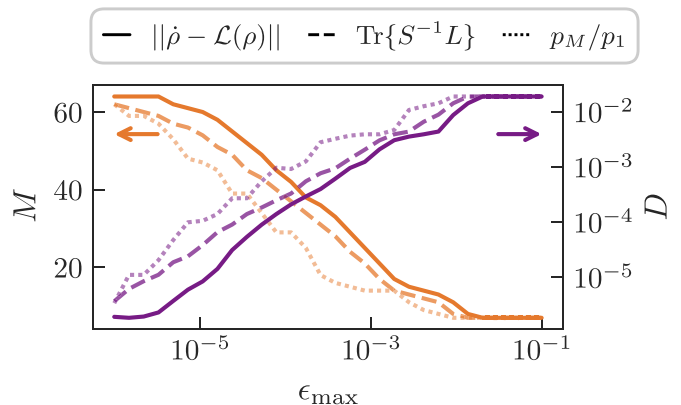


FIG. 3. Variation of the rank M and of the trace-distance D (between the true and approximated steady-state solutions) with the threshold ϵ_{\max} . We present results for all the choices of control parameter χ discussed in the text. The underlying physical model is the XYZ Heisenberg model with $N = 6$ spins and $J_y = 1$. The remaining physical parameters take the same values as in Fig. 4.

the error tolerance ϵ_{\max} , while the trace-distance D from the exact result steadily decreases.

C. Comparison with ensemble truncation methods

In this section, we outline the significant computational advantages that the LR-TDVP method offers over the ensemble truncation schemes discussed in Refs. [68–70]:

(1) Ensemble truncation methods execute linear algebra operations on $N_{\mathcal{H}} \times M(D + 1)$ matrices, leading to larger computational and storage demands than those required by our variational LR density matrix approach, which only requires storing matrices of size at most $N_{\mathcal{H}} \times M$.

(2) Ensemble truncation methods rely on a Kraus representation of the Liouvillian map. The operators decomposing this map are proportional to \sqrt{dt} , thereby restricting these methods to the explicit Euler first-order integration scheme. In Ref. [68], this difficulty is partially lifted by replacing the Kraus operator \hat{K}_0 with the full time-evolution operator $\hat{K}_0 = \exp(-iH_{\text{eff}}dt)$ and using a high-order integration scheme for its application. The contribution of the other Kraus operators to the dynamics is, however, still limited to an explicit first order in time Euler scheme. Conversely, our method allows integrating the EOM with a high-order adaptive-time-step solver. This approach not only significantly enhances the efficiency of our method but also offers greater accuracy and flexibility compared to the aforementioned schemes.

(3) Checks for basis inflation and deflation can be carried out at no additional costs to the simulation of our dynamics so that the additional diagonalization of an $M \times M$ matrix is only necessary when the deflation criterion is triggered. This is not the case in ensemble truncation methods which, for this purpose, require the diagonalization of an $M(D + 1) \times M(D + 1)$ matrix at every time step.

(4) Unlike ensemble truncation methods, where the selection of states to retain in the dynamics is heuristic in nature, our method's selection process is grounded in the time-dependent variational principle ensuring the adoption of the optimal LR basis at each time step.

III. NUMERICAL SIMULATIONS

In this section, we outline the significant computational advantages that our variational method offers over the ensemble truncation schemes discussed in Refs. [68–70] and demonstrate its applicability in a broad range of physical models.

Although a key strength of our method lies in its ability to capture the entire Liouvillian dynamics, we begin our analysis focusing on systems for which the relevant physics occurs in the steady state. Here we leverage our method only to reach stationarity, disregarding the remainder of the dynamics. In doing so, we showcase the method's effectiveness in analyzing steady-state phenomena in low-entropy systems. In Sec. III A, we investigate the dissipative phase transition in the anisotropic XYZ Heisenberg model. In Sec. III B, we apply our method to bosonic models, specifically to the study of the steady state of the bosonic simulator of the triangular antiferromagnetic Ising model. This exploration underscores the versatility and general-purposefulness of our approach.

We proceed to showcase the algorithm's capability to accurately capture the full Liouvillian dynamics, particularly in scenarios with nonmonotonous entropy profiles. In Sec. III C we provide insight into the mechanisms of basis inflation and deflation by studying the dynamics of the transverse-field Ising model in the presence of weak magnetic fields for which the system is known to be low rank. In Sec. III D, we address the timely problem of simulating the full dynamics of bias-preserving gates in dissipative cat qubit architectures displaying once again the advantage of a LR approximation.

A. Dissipative Heisenberg XYZ model

We consider a two-dimensional lattice consisting of N spin-1/2 particles governed by the Heisenberg XYZ Hamiltonian:

$$\hat{H} = \sum_{(i,j)} J_x \hat{\sigma}_i^x \hat{\sigma}_j^x + J_y \hat{\sigma}_i^y \hat{\sigma}_j^y + J_z \hat{\sigma}_i^z \hat{\sigma}_j^z + h_z \sum_j \hat{\sigma}_j^z, \quad (11)$$

where $\hat{\sigma}_i^\alpha$ ($\alpha = x, y, z$) are the Pauli operators acting on the i th spin of the lattice. The incoherent relaxation of each spin is described by the dissipator of $\hat{\sigma}_j^- = (\hat{\sigma}_j^x - i\hat{\sigma}_j^y)/2$, leading to the master equation:

$$\frac{\partial \hat{\rho}}{\partial t} = \mathcal{L}\hat{\rho} = -i[\hat{H}, \hat{\rho}] + \gamma \sum_{j=1}^N \mathcal{D}[\hat{\sigma}_j^-] \hat{\rho}. \quad (12)$$

This equation exhibits a \mathcal{Z}_2 symmetry, as evidenced by its invariance under the transformation $\hat{\sigma}_j^{x,y} \rightarrow -\hat{\sigma}_j^{x,y} \forall j$. In the thermodynamic limit, the steady state of the system bearing this symmetry is the fully aligned spin-down state $|\downarrow\rangle^{\otimes N}$. This state is characterized by having zero magnetization in the xy plane, a defining feature of the so-called *paramagnetic phase*.

In the presence of anisotropic coupling in the xy plane ($J_x \neq J_y$), and in the absence of any external field, however, relaxation and Hamiltonian processes compete with one another. This competition has been shown to induce a dissipative phase transition [39,86–99] spontaneously breaking the \mathcal{Z}_2 symmetry of the steady state and giving rise, in the thermodynamic limit, to an ordered phase with a nonvanishing in-plane magnetization, the so-called *ferromagnetic phase* [39,96,100–102].

In accordance with the conventions established in the relevant literature, all simulations of this model are performed fixing $J_x = 0.9$, $J_z = \gamma = 1$, and $h_z = 0$. In this section we vary J_y between 0.9 and 1.1 to investigate the transition from the paramagnetic to the ferromagnetic phase. Observing the transition in a fully quantum model that retains all correlations in the system is challenging. Indeed, the steady-state magnetization

$$M_y = \langle \hat{M}_y \rangle_{ss} = \frac{1}{N} \sum_j \langle \hat{\sigma}_j^y \rangle_{ss} \quad (13)$$

along the y direction, used as an order parameter in cluster mean-field studies [39], is always zero in the full model. Similarly, the homogeneous steady-state structure factor

$$S^{xx} = \frac{1}{N(N-1)} \sum_{i \neq j} \langle \hat{\sigma}_i^x \hat{\sigma}_j^x \rangle_{ss}, \quad (14)$$

which, in a Gutzwiller approximation is zero in the paramagnetic phase and acquires a positive value only in the ferromagnetic one [101], is not a good order parameter when correlations between different sites are included. Alternatives have been proposed, specifically, the angle-averaged magnetic susceptibility [100] and the trace-distance susceptibility [103]. The latter relies on the distance between steady-state matrices evaluated at infinitesimally close values of J_y and is thus too sensitive to any form of noise to be of use in approximated solutions. The former, however, would be well suited for our approximation. Its computation is, however, quite cumbersome, as it requires assessing the linear response of the system to small perturbations. Here, we thus prefer to present as an indicator of the transition the variation in J_y of

$$\Delta M_y = \sqrt{\langle \hat{M}_y^2 \rangle} = \sqrt{\frac{1}{N^2} \sum_{i,j} \langle \hat{\sigma}_i^y \hat{\sigma}_j^y \rangle}, \quad (15)$$

that is, the square root of the steady-state expectation value of the variance of \hat{M}_y . This is a good indicator of the long-range correlations developing in the array across the transition, and its derivative $\partial \Delta M_y / \partial J_y$ in J_y is a clear signature of critical behavior. We display this quantity in Fig. 4 for increasingly larger system sizes. A finite-size analysis in the linear lattice length $L = \sqrt{N}$ of the position of the maximum variance derivative yields an estimate of $J_c = 1.06 \pm 0.03$, consistent with the results obtained in Ref. [100]. The maxima of the curves themselves follow a power-law growth in L with critical exponent $\kappa = 0.92 \pm 0.08$. While the majority of the calculations were performed on Intel Xeon Platinum 8360Y CPUs, the most computationally intensive ones were executed on NVIDIA V100 GPUs.

To demonstrate the increasingly mixed character of the steady-state density matrix $\hat{\rho}_{ss}$, we display in Fig. 5 the steady-state von Neumann entropy

$$S = -\text{Tr}\{\hat{\rho}_{ss} \ln(\hat{\rho}_{ss})\}, \quad (16)$$

and its derivative $\partial S / \partial J_y$ as a function of J_y . As expected, we find that in proximity of the critical point, the entropy sharply rises with a slope that increases with the system size. Concurrently, $\partial S / \partial J_y$ shows a peaked structure which becomes increasingly more pronounced as we move towards the

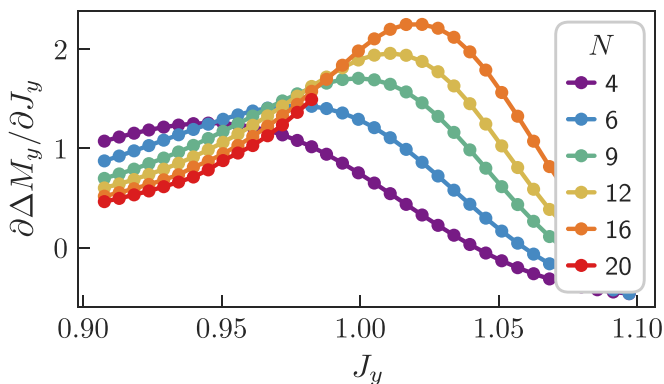


FIG. 4. Derivative in J_y of the variance ΔM_y of the magnetization along the y axis for systems with different numbers of spins: $N = 4$ (2×2 lattice), $N = 6$ (3×2), $N = 9$ (3×3), $N = 12$ (4×3), $N = 16$ (4×4), and $N = 20$ (5×4). Parameters: $J_x = 0.9$, $J_z = \gamma = 1$, and $h_x = 0$. For $N < 16$, where simulations are less demanding, we set $\epsilon_{\max} = 10^{-5}$. For $N \geq 16$, we set $\epsilon_{\max} = 10^{-4}$.

thermodynamic limit. By fitting the maximum entropy derivative with a power law in L [i.e., $\max(\partial S/\partial J_y) \propto L^\lambda$], we get an estimate for the critical exponent of $\lambda = 1.6 \pm 0.1$, again consistent with the state-of-the-art results found in Ref. [100] via the corner space method.

The system's steady state is obtained by numerically integrating Eq. (6) for a time $\gamma t = 15$ long enough for the system to reach stationarity. In all simulations, the rank is dynam-

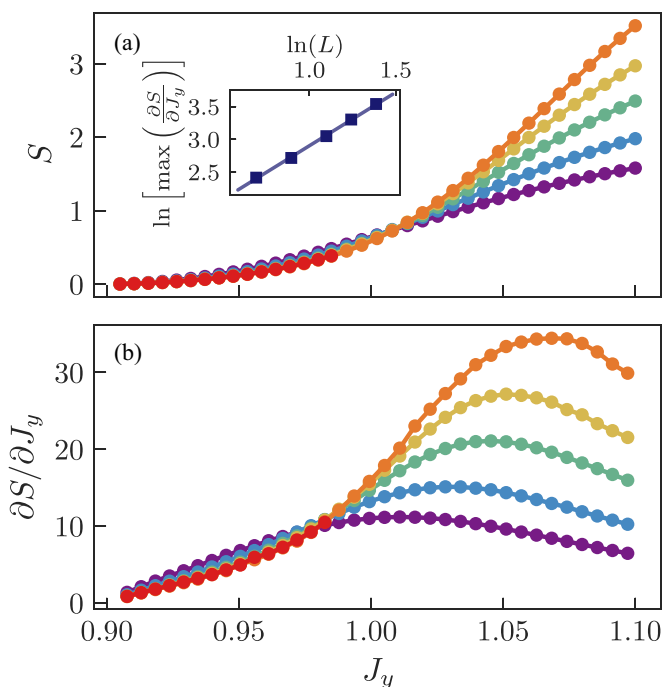


FIG. 5. Von Neumann entropy S and its derivative $\partial S/\partial J_y$ as a function of the coupling parameter J_y for lattices with different numbers of spins N (legend in Fig. 4). The inset displays the maximum value of the derivative as a function of the linear lattice length $L = \sqrt{N}$. The solid line is a power-law fit of the finite-size scaling. We use the same physical parameters as in Fig. 4.

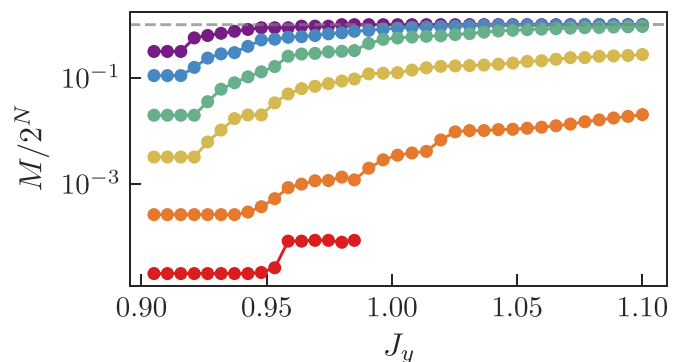


FIG. 6. Rank M of the steady state of the system as a function of the coupling strength J_y . For small values of J_y , i.e., small values of S , the rank of the system remains fixed at the initial preset value of $N + 1$. The rank increases with the entropy of the system according to the discussion in Sec. II B. We use the same physical parameters as in Fig. 4.

ically increased starting from an initial choice of $M(0) = N + 1$. As the initial state of the dynamics we take the pure state $|\psi(0)\rangle = |\downarrow\rangle^{\otimes N}$ setting to zero the population of the remaining N states making up the initial variational basis. These states are chosen as those with minimal Hamming distance from $|\psi(0)\rangle$.

As S increases, additional states are required to accurately describe $\hat{\rho}_{\text{ss}}$, thereby progressively reducing the computational advantage introduced by a LR ansatz. Given that S increases monotonically in J_y , the advantage introduced by our method is largest in proximity of the paramagnetic phase, where the entropy remains small. This is corroborated by Fig. 6, where we display $M(\gamma t = 15)$ as a function of J_y . Indeed, for highly entropic configurations [cf. Fig. 5(a)] $M \rightarrow 2^N$, i.e., the LR simulation becomes equivalent to the full solution of the master equation.

As a figure of merit for the method's computational performance we take the memory footprint of steady-state simulations similar to those performed above. The free parameters in this analysis are as follows:

- (i) The number of spins N , which uniquely determines the Hilbert space dimension.
- (ii) The coupling strength J_y , which uniquely determines the system's configuration. Recall that all other physical parameters have been fixed.
- (iii) The dimension M of the LR space. This can be fixed at the start, as we will do in what follows, or varied dynamically, in which case the free parameter becomes the threshold ϵ_{\max} .

For a synthetic two-dimensional representation of the results—memory footprint against Hilbert space dimension—as depicted in Fig. 7, both J_y and M need to be fixed. We fix $J_y = 0.98$ and select M , for each value of N , so as to ensure that the relative error in the estimation of M_z remains within a 0.1% margin from the actual solution. The distance between the LR estimate and the true value of M_z for different lattice sizes is shown in the inset to Fig. 7. While for $N < 16$ the true value of M_z is obtained via numerical integration of the full master equation, for $N = 16$ we resort to the Monte Carlo trajectory method, averaging over 10^4 trajectories. The results, as illustrated in Fig. 7, highlight the significant computational

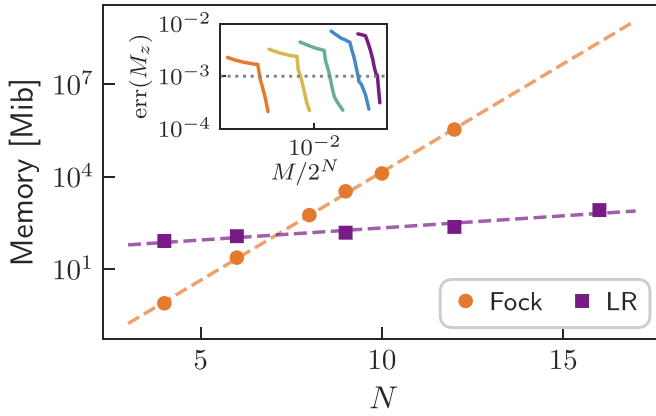


FIG. 7. Memory allocations as a function of number of simulated spins N for the full simulation and the LR-TDVP one. We set the value of $J_y = 0.98$. For each value of N , we choose the rank M ensuring the relative error on the magnetization M_z to be smaller than 0.1%, namely $\text{err}(M_z) = |M_z^{\text{full}} - M_z^{\text{LR}}|/|M_z^{\text{full}}| \leq 10^{-3}$. The inset shows the behavior of $\text{err}(M_z)$ as a function of M . The color scheme in the inset is the same as in Fig. 4, as are all physical parameters aside from J_y .

advantages of our approach. The LR-TDVP method not only accurately captures all the critical features of the XYZ model but also demonstrates improved efficiency in terms of memory usage and computation time compared to both the full solution and the dynamical truncation schemes referenced in Refs. [68–70].

In concluding this section, it is important to stress that our method is inherently dynamic in nature. As such, it is not expected to always outperform methods specifically tailored for solving steady-state problems. For instance, when compared to the corner space renormalization method, which serves as our reference, the LR-TDVP does not surpass it in terms of the system sizes that can be explored. The corner space method, based on spatial block decimation, is indeed very effective for systems with spatial translational invariance.

One of the key advantages of the LR-TDVP method over the corner space approach, however, is its generality and applicability to a broader range of low-entropy systems, not limited to those characterized by translational invariance. Additionally, this method offers more precise control over error estimation and convergence in the rank. In contrast, the corner space method's truncation at any decimation level introduces errors that, while locally controllable, can accumulate and propagate through different decimation steps, affecting the overall accuracy. This often necessitates running multiple simulations with varying truncation combinations to ensure convergence—a requirement not present in our algorithm.

Furthermore, the merging process in the corner space method is not unique and can lead to artificially slow timescales, potentially affecting performance. The fixed but nonunique choice of basis in the corner space method depends on the initial lattice for decimation, meaning that missing a crucial state in the system can lead to erroneous or artificially slow simulations. Conversely, our algorithm allows for a more precise final result, even if part of the dynamics might be initially missed. Error control is much more straightforward and

can be dynamically adjusted by expanding the LR dimension. This flexibility offers a distinct advantage in terms of precision and control over the simulation process.

In summary, while the LR-TDVP method may not always surpass specialized steady-state solvers in terms of system size exploration, it compensates with its generality, error control, and adaptability. This makes it a valuable tool for studying a wide range of low-entropy quantum systems, including those with nonuniform interactions where methods like the corner space renormalization may not be applicable.

B. Frustrated antiferromagnetism in quadratically driven QED cavities

We consider an array of $N = 2, 3$ coupled dissipative quadratically driven QED nonlinear cavities: a bosonic model known to be a valid quantum simulator of the triangular antiferromagnetic Ising model [99,104–106]. The Hamiltonian of the model reads

$$\hat{H} = \sum_{j=1}^N -\Delta \hat{a}_j^\dagger \hat{a}_j + \frac{U}{2} \hat{a}_j^{\dagger 2} \hat{a}_j^2 + \frac{G}{2} \hat{a}_j^{\dagger 2} + \frac{G^*}{2} \hat{a}_j^2 - \sum_{j \neq j'} \frac{J}{2} (\hat{a}_j^\dagger \hat{a}_{j'} + \hat{a}_j \hat{a}_{j'}^\dagger), \quad (17)$$

where U is the Kerr nonlinearity, G the two-photon driving field amplitude, Δ the resonators' detuning frequency, and J the hopping coefficient. We include single- and two-body losses with rates γ and η , respectively, so that the system evolves according to the Lindblad master equation,

$$\frac{\partial \hat{\rho}}{\partial t} = \mathcal{L} \hat{\rho} = -i[\hat{H}, \hat{\rho}] + \sum_j (\gamma \mathcal{D}[\hat{a}_j] + \eta \mathcal{D}[\hat{a}_j^2]) \hat{\rho}. \quad (18)$$

In the limit of a strong driving field, the photons in each cavity form a coherent state with phase α or $-\alpha$. While a positive hopping coefficient $J > 0$ favors the formation of a statistical mixture of two equiprobable separable coherent states [107] $|\Psi_\pm\rangle = \prod_j |\pm\alpha\rangle_j$, a negative one $J < 0$ favors the emergence of states $|\Phi_\pm\rangle = |\pm\alpha, \mp\alpha, \pm\alpha, \mp\alpha, \dots\rangle$ with an antisymmetric alignment of phases. The two limits map directly onto the ferromagnetic and antiferromagnetic configuration of the effective spin model via the transformation $|\alpha\rangle \rightarrow |\uparrow\rangle$ and $|\alpha\rangle \rightarrow |\downarrow\rangle$.

Following Ref. [105], we investigate the effective antiferromagnetic spin model by studying the steady-state properties of the photonic system for varying values of G . Specifically, we focus on the steady-state values of the first-order coherence correlation function,

$$g_{1,2}^{(1)} = \langle \hat{a}_1^\dagger \hat{a}_2 \rangle / \langle \hat{a}_1^\dagger \hat{a}_1 \rangle, \quad (19)$$

and of the von Neumann entropy S defined in Eq. (16). Our results, displayed in Fig. 8, are consistent with the findings in Ref. [105]. Indeed, as expected for an antiferromagnetic coupling, the correlation $g_{1,2}^{(1)}$ for $N = 2$ is negative and, for increasing values of G , converges to the asymptotic value $g_{1,2}^{(1)} = -1$. Concurrently, the entropy increases from $S(G = 0) = 0$ to $S(G \gg \gamma) = \ln(2)$, consistently with the double degeneracy of the ground-state manifold of the equivalent spin model.

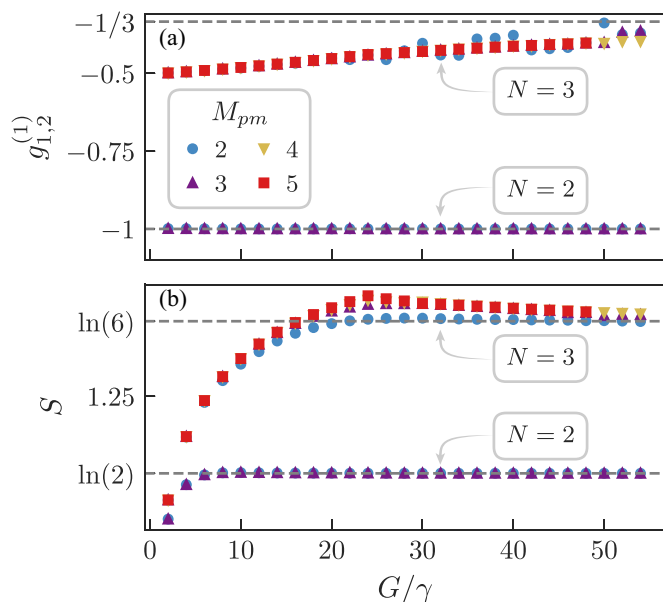


FIG. 8. The first-order correlation function $g_{1,2}^{(1)}$ (a) and the von Neumann entropy S (b) as a function of the amplitude of the two-photon driving G for the systems with $N = 2, 3$ cavities. Dashed gray lines are used to display the expected plateau values of the different quantities in the limit of large driving. Parameters: $\gamma = \eta = 1$, $U = 10$, and $\Delta = J = -10$.

For an odd number of sites, the presence of geometrical frustration in the system hinders the emergence of $|\Phi_{\pm}\rangle$ states in the open system delaying to larger values of G the onset of the antiferromagnetic signatures. The effects of frustrations are visible for $N = 3$ in the nonmonotonous behavior of S as a function of G and in its asymptotic value of $S = \ln(6)$. Indeed, the latter is consistent with the existence of six possible spin configurations, emerging as a result of frustration and minimizing the energy of the equivalent spin model.

We obtained all results by numerically integrating Eq. (6) over a time interval sufficiently long to allow the system to reach the steady state. The Hilbert space of the N cavities is obtained as the N -fold tensor product of truncated single-boson Fock spaces. For numerical convenience, we adjusted the truncation dimension according to the prescription $N_{\text{cut}}(G) = \max\{10, 5G/W\}$, where $W = \sqrt{U^2 + \eta^2}$. For $N = 2$, a LR subspace of dimension $M = (M_{\text{pm}})^N$ with $M_{\text{pm}} = 2$ (number of states per mode) accurately captures the relevant physics, as evidenced by the indistinguishable results obtained for $M_{\text{pm}} = 3$. For $N = 3$, a larger LR space is necessary. We present results for $M_{\text{pm}} = 2, 3, 4, 5$. Convergence is observed for $M_{\text{pm}} \geq 3$.

Direct numerical integration of Eq. (18) for determining the steady state of the system quickly becomes impractical, as highlighted by the extensive efforts in Ref. [105]. In that approach, the steady state is computed by numerically solving $\partial_t \hat{\rho} = 0$, a linear system of up to 10^8 equations. In contrast, our method demonstrates significant potential by efficiently computing the steady state by integration of Eq. (18) but retaining only a small number of optimal states. This approach not only reduces computational complexity but also maintains

accuracy, showcasing the advantages of our method in handling large-scale quantum systems.

C. Transverse-field Ising model

In this section, we demonstrate our algorithm's ability to accurately capture the full dynamics of a system while efficiently adapting to an entropy profile that does not monotonically increase over time. Specifically, we examine a scenario where the entropy initially rises, reaches a peak at t_{max} with a maximum value S_{max} , and then decreases towards a steady-state value $S_{\text{ss}} < S_{\text{max}}$.

This behavior is exemplified in the transverse-field Ising model [$J_x = J_y = 0$, $J_z = \gamma = 1$, and $h_x > 0$ in Eqs. (11) and (12)] which is characterized by a dynamics that, under specific initial conditions, remains LR at all times. Indeed, for sufficiently small values of h_x in (11), the steady state of the model closely resembles that at $h_x = 0$, which reads $|\psi_0\rangle = |\downarrow\rangle^{\otimes N}$. Consequently, an evolution under small h_x starting from the latter state exhibits the desired entropy profile while remaining amenable to a LR representation. In contrast, an evolution starting from the state $|\uparrow\rangle^{\otimes N}$ would saturate the rank, rendering the LR ansatz an inefficient choice.

In Fig. 9(a), we display the time evolution of the structure factor ΔM_y as defined in Eq. (15). We remark the perfect agreement between the LR and full simulations.

Figure 9(b) depicts the desired evolution of the system's entropy and highlights the dynamic adaptation of the rank $M(t)$ to its changes throughout the simulation. Specifically, $M(t)$ initially increases, in parallel with S , to maintain the accuracy threshold set by ϵ_{max} . However, for $t > t_{\text{max}}$, as S decreases, M is automatically reduced, thereby enhancing computational efficiency.

In Fig. 9(c), we display the variational error χ , as defined in Eq. (10), which serves as a measure of the error performed at time t . As expected, the automatic adaptation of M ensures that $\epsilon_{\text{min}} < \chi(t) < \epsilon_{\text{max}}$. In contrast, when the rank is fixed to either $M_{\text{max}} = \max_t[M(t)]$ or $M_{\text{min}} = \min_t[M(t)]$, there exist regions where $\chi(t)$ falls below ϵ_{min} or exceeds ϵ_{max} , respectively.

D. Cat qubit gates

In this section we apply a LR ansatz on dissipative cat qubit architectures [19,20,108–115], taking full advantage of the potentialities of our method to simulate bias-preserving logical operations [111,114,116,117].

1. Definition of dissipative cat qubits

Schrödinger cat qubits [19,111–115,118–126] encode information as a symmetric pattern in phase space, specifically, within the subspace $\{|\mathcal{C}_{\alpha}^{+}\rangle, |\mathcal{C}_{\alpha}^{-}\rangle\}$ spanned by cat states of opposite parity [111,116], where

$$|\mathcal{C}_{\alpha}^{\pm}\rangle = \frac{|\alpha\rangle \pm |-\alpha\rangle}{2\sqrt{1 \pm e^{-2|\alpha|^2}}}, \quad (20)$$

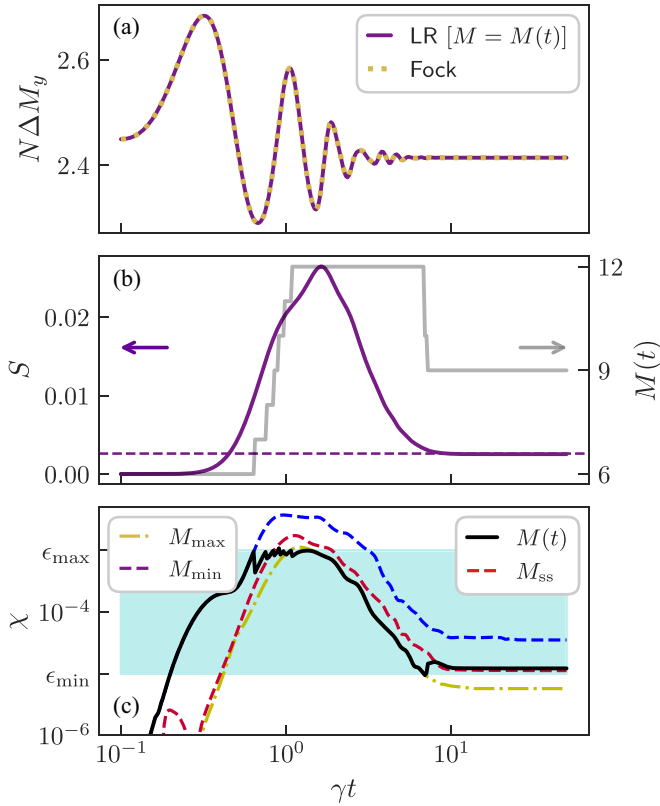


FIG. 9. Example of low-rank dynamics in the transverse-field Ising model. (a) Time evolution of the standard deviation ΔM_y of the spin correlation along y . (b) Evolution of the system's entropy S (left axis) and of the adaptive rank $M(t)$ (right axis). The dashed blue line indicates the true steady-state value of S . (c) Evolution of the approximated variational error χ [Eq. (10)] for different choices of the rank, both changing and static in time. The shaded blue region marks the interval $\epsilon_{\min} < \chi < \epsilon_{\max}$. Parameters: $J_x = J_y = 0$, $J_z = \gamma = 1$, $h_x = 0.75$, $N = 6$, $\epsilon_{\min} = 10^{-5}$, $\epsilon_{\max} = 10^{-3}$, $M_{\min} = M(0) = 6$, $M_{\max} = 12$, and $M_{\text{ss}} = M(\gamma t = 50) = 9$.

and $\hat{a}|\alpha\rangle = \alpha|\alpha\rangle$ [107,127]. Within this manifold, the prevailing convention defines the logical states as

$$\begin{aligned} |0\rangle &= \frac{1}{\sqrt{2}}(|\mathcal{C}_\alpha^+\rangle + |\mathcal{C}_\alpha^-\rangle) \approx |\alpha\rangle + \mathcal{O}e^{-2|\alpha|^2} \\ |1\rangle &= \frac{1}{\sqrt{2}}(|\mathcal{C}_\alpha^+\rangle - |\mathcal{C}_\alpha^-\rangle) \approx |-\alpha\rangle + \mathcal{O}e^{-2|\alpha|^2}, \end{aligned} \quad (21)$$

so that $|\pm\rangle = (|0\rangle \pm |1\rangle)/\sqrt{2} = |\mathcal{C}_\alpha^\pm\rangle$. In what follows we will assume $\alpha \in \mathbb{R}$.

Generating and stabilizing this manifold is far from trivial, as it requires engineering parity-preserving processes involving exclusively the pairwise exchange of photons between the system and its environment [111,114,116,117]. In dissipative cat qubits, for instance, this manifold coincides with the four-degenerate steady-state manifold of the dissipator $\mathcal{L}_0 = \kappa_2 \mathcal{D}[\hat{a}^2 - \alpha^2]$, modeling engineered two-photon drive and dissipation processes [16,19,20,109–111,128]. Indeed, because of the underlying strong \mathcal{Z}_2 symmetry of the Liouvillian, the right kernel of \mathcal{L}_0 is [16,113,129,130]

$$\text{As}(\mathcal{H}) = \lim_{t \rightarrow \infty} e^{\mathcal{L}_0 t} \text{Op}(\mathcal{H}) = \text{Span} \left(\{ |\mathcal{C}_\alpha^\mu\rangle \langle \mathcal{C}_\alpha^\nu| \}_{\mu, \nu = \pm} \right), \quad (22)$$

so that, for any choice of $\hat{\rho}_0$,

$$\hat{\rho}_{\text{ss}} = \lim_{t \rightarrow \infty} e^{\mathcal{L}_0 t} \hat{\rho}_0 = \sum_{\mu, \nu = \pm} c_{\mu, \nu} |\mathcal{C}_\alpha^\mu\rangle \langle \mathcal{C}_\alpha^\nu|. \quad (23)$$

The coefficients $c_{\mu, \nu}$ encode the quantum information and are defined as

$$c_{\mu, \nu} = \text{Tr} \{ \hat{J}_{\mu, \nu}^\dagger \hat{\rho}_0 \}, \quad (24)$$

where the operators $\hat{J}_{\mu, \nu}$, spanning the left kernel of \mathcal{L}_0 , are defined as [111,130]

$$\begin{aligned} \hat{J}_{++} &= \sum_{n=0}^{\infty} |2n\rangle \langle 2n|, \\ \hat{J}_{--} &= \sum_{n=0}^{\infty} |2n+1\rangle \langle 2n+1|, \\ \hat{J}_{+-} &= \hat{J}_{-+} = \mathcal{A}_\alpha \sum_q a_q \hat{J}_{+-}^{(q)}. \end{aligned} \quad (25)$$

Here

$$\begin{aligned} \mathcal{A}_\alpha &= \sqrt{\frac{2\alpha^2}{\sinh(2\alpha^2)}}, \quad a_q = \frac{(-1)^q}{2q+1} I_q(\alpha^2), \\ \hat{J}_{+-}^{(q)} &= \begin{cases} (\hat{a}^\dagger \hat{a} - 1)!! \hat{J}_{++} \hat{a}^{2q+1} & (q \geq 0) \\ \hat{J}_{++} (\hat{a}^\dagger + 2q)!! & (q = 0) \\ \hat{J}_{++} (\hat{a}^\dagger)^{2|q|-1} \frac{(\hat{a}^\dagger \hat{a})!!}{(\hat{a}^\dagger \hat{a} + 2|q| - 1)!!} & (q < 0) \end{cases}, \end{aligned} \quad (26)$$

where $I_q(\cdot)$ is the modified Bessel function of the first kind and $n!! = n \cdot (n-2)!!$ is the double factorial, applied elementwise to all diagonal operators.

The two-photon drive and dissipation processes modelled by \mathcal{L}_0 have been realized, for example, on superconducting circuit platforms. In these platforms, the dominant source of errors comes from single photon loss processes, modeled by the dissipator $\kappa_1 \mathcal{D}[\hat{a}]$ with $\kappa_1/\kappa_2 \ll 1$. These processes hinder the code's ability to encode quantum information as well as the performance of logical gates [4,124,128].

2. Z, ZZ, and ZZZ gates

Let us consider the application of Z rotations of an angle π over $N = 1, 2, 3$ cat qubits. For a single qubit, these rotations are equivalent to the application of a logical Pauli $\hat{\sigma}^z$ operator, which introduces a phase of (-1) on the logical $|1\rangle$ state [131]. In the cat basis, this amounts to exchanging $|\mathcal{C}_\alpha^+\rangle$ and $|\mathcal{C}_\alpha^-\rangle$. Similarly, in multiqubit systems, these rotations correspond to a unitary transformation changing the tensor product $|\mathcal{C}_\alpha^\pm\rangle \dots |\mathcal{C}_\alpha^\pm\rangle$ into $|\mathcal{C}_\alpha^\mp\rangle \dots |\mathcal{C}_\alpha^\mp\rangle$.

Logical Z operations can be approximately implemented by evolving the system for a time T under the Liouvillian $\mathcal{L} = \mathcal{L}_0 + \mathcal{L}_1$ given by [111,112,124,125,128]:

$$\begin{aligned} \mathcal{L}_0 &= \sum_{i=1}^N \kappa_2 \mathcal{D}[\hat{a}_i^2 - \alpha_i^2], \\ \mathcal{L}_1 \hat{\rho} &= -i[\hat{H}_Z, \hat{\rho}] + \sum_{i=1}^N \kappa_1 \mathcal{D}[\hat{a}_i] \hat{\rho}. \end{aligned} \quad (27)$$

Here \mathcal{L}_1 encompasses both the unwanted single body losses that compromise the accuracy of gate operations, and the ideal Hamiltonian evolution responsible for the rotation. Specifically, the Hamiltonian \hat{H}_Z is defined as [123,132]:

$$\hat{H}_Z = \begin{cases} \epsilon_Z(\hat{a}_1 + \hat{a}_1^\dagger) & (N = 1) \\ \epsilon_{ZZ}(\hat{a}_1\hat{a}_2^\dagger + \hat{a}_1^\dagger\hat{a}_2) & (N = 2) \\ \epsilon_{ZZZ}(\hat{a}_1\hat{a}_2\hat{a}_3^\dagger + \hat{a}_1^\dagger\hat{a}_2^\dagger\hat{a}_3) & (N = 3) \end{cases} \quad (28)$$

with

$$\epsilon_Z = \frac{\pi}{4\alpha T}, \quad \epsilon_{ZZ} = \frac{\pi}{4\alpha^2 T}, \quad \epsilon_{ZZZ} = \frac{\pi}{4\alpha^3 T}. \quad (29)$$

If we initialize each qubit in the $|+\rangle$ state then, ideally, after a time T , all qubits should be in the $|-\rangle$ state, for which $\langle -|\hat{J}_{++}|-\rangle = 0$. Therefore, we can use

$$P_Z = \left\langle \bigotimes_{i=1}^N \hat{J}_{++} \right\rangle \Big|_{t=T} \quad (30)$$

as a measure of the phase-flip error probability during the Z rotation. Figure 10(a) displays P_Z as a function of α^2 . Simulations were conducted in a truncated Fock space with dimension $N_{\text{cut}}(\alpha) = \max\{20, \lceil 4.5\alpha^2 \rceil\}$, ensuring the convergence of each data point. Notably, the L simulations, executed with $M_{\text{pm}} = 3$ states per mode, overlay perfectly with the results obtained from the full evolution. Simulations for $N = 3$ were restricted to $\alpha^2 < 5$ because of prohibitively large memory requirements.

Conversely, since any rotation leaves the states lying on the rotation axis unchanged, if we initialize each qubit in $|0\rangle \approx |\alpha\rangle$, we expect to find them in that exact same state after evolving under \mathcal{L} for a time T . As a quantifier of the bit-flip error rate affecting the system we can therefore take

$$P_X = 1 - \left\langle \bigotimes_{i=1}^N \text{sgn}(\hat{x}) \right\rangle \Big|_{t=T}, \quad (31)$$

where $\hat{x} = \hat{a} + \hat{a}^\dagger$ and $\text{sgn}(\hat{x}) \approx \hat{J}_{+-}$. In Fig. 10(b) we display P_X as a function of α^2 . Noticeably, our model is able to accurately capture P_X even up to the very small error probabilities associated with its exponential suppression in α^2 [19,111,113,114]. The suppression coefficients ζ extracted from an exponential fit of the exact simulations are $\zeta = 2.13 \pm 0.01$, 2.13 ± 0.01 , and 2.16 ± 0.03 , respectively, for $N = 1, 2, 3$. The same fit on the LR data yields $\zeta = 2.13 \pm 0.01$, 2.14 ± 0.01 , and 2.14 ± 0.02 . These estimates are in agreement with each other and with the theoretical expectation [123]. As we show in the inset of Fig. 10(b), the entropy S of the target state at time T decreases with the number of photons in the system. This entails that progressively less states are necessary to capture the dynamics. To avoid overrepresentation in our LR ansatz we thus reduce M_{pm} (number of states per mode included in the simulation) with the photon number. Specifically, we obtain good agreement with the full solution by taking $M_{\text{pm}} = 1$ for $\alpha^2 > 6$.

IV. CONCLUSIONS

We introduce a model-independent method designed for the efficient simulation of the dynamics of low-entropy

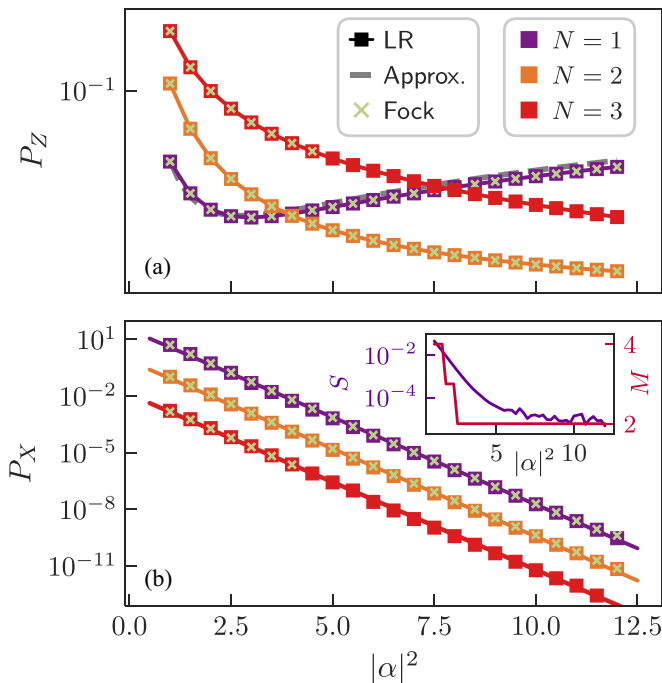


FIG. 10. Error probabilities of N -qubit Z gates, with $N = 1, 2, 3$. (a) Phase-flip error probability P_Z [Eq. (30)] as a function of the photon number α^2 . We display as a dashed gray line the analytical approximation $P_Z \approx \kappa_1 T \alpha^2 + \epsilon_Z^2 T / \alpha^2$ (for $N = 1$) provided in Ref. [123]. (b) Bit-flip error probability P_X [Eq. (31)] as a function of the photon number α^2 . To improve visualization, as the curves would largely overlap, we multiply each curve by a different constant, effectively shifting them vertically on the plot. The constants are $R = 10^2, 1, 10^{-2}$ for $N = 1, 2, 3$, respectively. Full lines are used to display the exponential fit of the LR data. Because of computational constraints, the exact simulations for $N = 3$ were only possible up to $\alpha^2 = 5$. The inset shows the von Neumann entropy S at time T as a function of α^2 for $N = 1$. In both panels, the results obtained from the L simulations (squares) are in agreement with the full solution (yellow crosses). Parameters: $\kappa_2 = 1$, $\kappa_1 = 1/1000$, and $\epsilon_Z = \epsilon_{ZZ} = \epsilon_{ZZZ} = 1/20$.

systems. Recognizing that such evolution can be accurately captured by a limited number of states, our method builds on and advances the previously established ensemble truncation schemes [68–71], integrating their key features within the framework of the time-dependent variational principle recently developed for open quantum systems [48,72–74]. Our approach enhances previous ensemble truncation methods by offering a rigorous and systematic protocol for defining and dynamically modifying the low-rank basis. Furthermore, it extends prior variational descriptions of dissipative systems by introducing a computationally efficient protocol for adapting the size of the variational manifold, thereby dynamically adjusting the rank of the density matrix throughout the simulation. This dynamic adaptation ensures that the low-rank subspace of the Hilbert space optimally represents the system's state at all times.

We have conducted extensive benchmarking of our method across various model systems that have garnered significant attention in recent decades. Particularly noteworthy is its application to multiqubit bosonic codes [19,111–115,118–126],

which are emerging as promising candidates for fault-tolerant quantum hardware.

To ensure easy integration into diverse research workflows, we have implemented our method in Julia [81] and incorporated it into the QuantumToolbox library [80,82], a comprehensive toolkit for quantum system simulation.

Looking ahead, potential extensions of our work include the incorporation of efficient variational representations of the low-rank space, such as tensor-network [47,133] or neural quantum states [134]. These advancements could enable the simulation of larger-scale systems. Additionally, our variational approach could be adapted to the simulation of the master equation of non-Markovian open quantum systems, such as the Bloch-Redfield master equation and subsequent evolutions [135]. A non-Markovian description of the dynamics is necessary in many scenarios of increasing importance for quantum technologies, where the Markovian and secular approximations leading to the Lindblad form [136] break down. Last, a digital version of our method could approximate the simulation of noisy quantum computing hardware, potentially enhancing error-mitigation protocols that rely on estimating hardware-specific noisy quantum channels [137–139].

ACKNOWLEDGMENTS

We acknowledge several fruitful discussions with Fabrizio Minganti, Alberto Mercurio, and Lorenzo Fioroni. We are grateful to Tim Besard for providing useful insight into the GPU porting of the method. This study received funding entirely or partially from the Swiss National Science Foundation (SNSF) Projects No. 200020_185015, No. 200020_215172, No. 20QU-1_215928, and from the EPFL Science Seed Fund 563276 2021.

APPENDIX A: DERIVATION OF EQ. (6)

Given the generic parametrization $\hat{\rho}(t) = \hat{\rho}[\theta(t)]$, the EOM for the parameters θ that at each time best approximate the action of \mathcal{L} on $\hat{\rho}$ are obtained by minimizing the Frobenius distance between the variational evolution and the physical one. This is ensured by requiring the variation of this quantity to vanish, that is, by imposing

$$\delta \left\| \left(\frac{d}{dt} - \mathcal{L} \right) \hat{\rho} \right\|^2 = 0. \quad (\text{A1})$$

Note that in this notation the time derivative d/dt is intended with respect to the variational parameters, i.e.,

$$\dot{\hat{\rho}} = \frac{d\hat{\rho}}{dt} = \nabla_{\theta} \hat{\rho}(\theta) \cdot \dot{\theta} = \sum_j \frac{\partial \hat{\rho}}{\partial \theta_j} \dot{\theta}_j. \quad (\text{A2})$$

With this definition, Eq. (A1) can be rewritten as (see Ref. [48] for the full derivation)

$$\begin{aligned} 0 &= \delta \{ \text{Tr} \{ [\dot{\hat{\rho}} - \mathcal{L}(\hat{\rho})]^\dagger [\dot{\hat{\rho}} - \mathcal{L}(\hat{\rho})] \} \} \\ &= \text{Tr} \left\{ \left(\frac{\partial \hat{\rho}}{\partial \theta_i} \right)^\dagger \left[\sum_j \frac{\partial \hat{\rho}}{\partial \theta_j} \dot{\theta}_j - \mathcal{L}(\hat{\rho}) \right] \right\} \delta \dot{\theta}_i^* + \text{H.c.}, \quad (\text{A3}) \end{aligned}$$

so that

$$\text{Tr} \left\{ \left(\frac{\partial \hat{\rho}}{\partial \theta_i} \right)^\dagger [\dot{\hat{\rho}} - \mathcal{L}(\hat{\rho})] \right\} = 0 \quad (\text{A4})$$

for all choices of i . This is equivalent to the Dirac and Frenkel variational principle, where the projection of the stochastic evolution onto the tangent subspace $\{\partial \hat{\rho} / \partial \theta_i\}_i$ is made to vanish.

Equation (5) results from incorporating the Lagrange multiplier λ into Eq. (A1), thereby embedding trace preservation directly into the EOM. Analogous calculations as those presented above lead from Eq. (5) to

$$0 = \text{Tr} \left\{ \left(\frac{\partial \hat{\rho}}{\partial \theta_i} \right)^\dagger \left[\sum_j \frac{\partial \hat{\rho}}{\partial \theta_j} \dot{\theta}_j - \mathcal{L}(\hat{\rho}) + \lambda \mathbb{1} \right] \delta \dot{\theta}_i^* + \text{H.c.} \right\}, \quad (\text{A5})$$

where choosing the constraint $\frac{d}{dt} \text{Tr} \{ \hat{\rho} + \hat{\rho}^\dagger \}$, over the more obvious choice $\frac{d}{dt} \text{Tr} \{ \hat{\rho} \}$, preserves the symmetry under complex conjugation found in Eq. (A3). Because of this, Eq. (A5) unambiguously results in

$$\text{Tr} \left\{ \left(\frac{\partial \hat{\rho}}{\partial \theta_i} \right)^\dagger [\dot{\hat{\rho}} - \mathcal{L}(\hat{\rho}) + \lambda \mathbb{1}] \right\} = 0 \quad (\text{A6})$$

for all choices of i .

Consider now the specific LR ansatz in Eq. (3), for which the variational parameters are the populations B_{ij} and the coefficients $z_{\alpha k}$. For the populations B_{ij} , Eq. (A6) amounts to

$$\begin{aligned} 0 &= \text{Tr} \left\{ \left(\frac{\partial \hat{\rho}}{\partial B_{ij}} \right)^\dagger [\dot{\hat{\rho}} - \mathcal{L}(\hat{\rho}) + \lambda \mathbb{1}] \right\} \\ &= \langle \varphi_i | \dot{\hat{\rho}} - \mathcal{L}(\hat{\rho}) + \lambda \mathbb{1} | \varphi_j \rangle \\ &= \langle \varphi_i | \dot{\hat{\rho}} - \mathcal{L}(\hat{\rho}) | \varphi_j \rangle + \lambda S_{ij} \\ &= (\mathbf{S} \dot{\mathbf{B}} \mathbf{S} + \boldsymbol{\tau} \mathbf{B} \mathbf{S} + \mathbf{S} \mathbf{B} \boldsymbol{\tau}^\dagger - \mathbf{L})_{ij} + \lambda S_{ij}, \quad (\text{A7}) \end{aligned}$$

where the last equality follows from substituting

$$\dot{\hat{\rho}} = \sum_{l,m} \dot{B}_{lm} |\varphi_l\rangle \langle \varphi_m| + B_{lm} |\dot{\varphi}_l\rangle \langle \varphi_m| + B_{lm} |\varphi_l\rangle \langle \dot{\varphi}_m|, \quad (\text{A8})$$

as detailed in the calculations in Ref. [74]. Upon isolating $\dot{\mathbf{B}}$ in Eq. (A7), we get

$$\dot{\mathbf{B}} = \mathbf{S}^{-1} \mathbf{L} \mathbf{S}^{-1} - (\mathbf{S}^{-1} \boldsymbol{\tau} \mathbf{B} + \mathbf{B} \boldsymbol{\tau}^\dagger \mathbf{S}^{-1}) - \lambda \mathbf{S}^{-1}, \quad (\text{A9})$$

where $\boldsymbol{\tau} = \mathbf{z}^\dagger \mathbf{z}$ and, as explained in the main text, \mathbf{S}^{-1} and \mathbf{B}^{-1} are the pseudoinverse matrices of respectively \mathbf{S} and \mathbf{B} . The value of λ is determined by the constraint

$$\begin{aligned} 0 &= \frac{d}{dt} \text{Tr} \{ \hat{\rho} \} = \text{Tr} \{ \dot{\mathbf{B}} \mathbf{S} + (\boldsymbol{\tau} + \boldsymbol{\tau}^\dagger) \mathbf{B} \} \\ &= \text{Tr} \{ \mathbf{S}^{-1} \mathbf{L} - \lambda \}, \quad (\text{A10}) \end{aligned}$$

from which $\lambda = \text{Tr} \{ \mathbf{S}^{-1} \mathbf{L} \} / \text{Tr} \{ \mathbb{1} \} = \text{Tr} \{ \mathbf{S}^{-1} \mathbf{L} \} / M$.

Equation (A9) is general and holds for any analytical parametrization of the LR states. The variational equation for the coefficients $z_{\alpha k}$ as presented in Eq. (A6), on the other hand, is explicitly dependent on the choice of parametrization. For the full parametrization in Eq. (4), in particular, it can be

similarly reformulated as

$$\begin{aligned}
0 &= \text{Tr} \left\{ \left(\frac{\partial \hat{\rho}}{\partial z_{\alpha k}^*} \right)^\dagger [\dot{\hat{\rho}} - \mathcal{L}(\hat{\rho}) + \lambda \mathbb{1}] \right\} \\
&= \sum_{j, \beta} \langle e_\alpha | \dot{\hat{\rho}} - \mathcal{L}(\hat{\rho}) + \lambda \mathbb{1} | e_\beta \rangle B_{jk} z_{\beta j} \\
&= \sum_{j, \beta} B_{jk} z_{\alpha j} \langle e_\alpha | \dot{\hat{\rho}} - \mathcal{L}(\hat{\rho}) | e_\beta \rangle + \lambda (z\mathbf{B})_{\alpha k} \\
&= [z\dot{\mathbf{B}}\mathbf{S}\mathbf{B} + z\mathbf{B}\mathbf{S}\dot{z} + z\mathbf{B}z^\dagger z\mathbf{B} - (\mathbf{L} - \lambda \mathbb{1})z\mathbf{B}]_{\alpha k},
\end{aligned} \tag{A11}$$

where the last equality follows once again from Eq. (A8). Multiplying by \mathbf{B}^{-1} on the right, and substituting Eq. (A9) for $\dot{\mathbf{B}}$, we find that

$$(\mathbb{1} - \mathbf{P})z\mathbf{B}\mathbf{S} = (\tilde{\mathbf{L}} - z\mathbf{S}^{-1}\mathbf{L}), \tag{A12}$$

where $\mathbf{P} = z\mathbf{S}^{-1}z^\dagger$ is the projector on the LR manifold. Since by definition $\mathbf{P}z = 0$, the latter reduces to

$$z = (\tilde{\mathbf{L}} - z\mathbf{S}^{-1}\mathbf{L})\mathbf{S}^{-1}\mathbf{B}^{-1}. \tag{A13}$$

A few comments on the full parametrization are now in order. First, it is evident from Eq. (A13) that $\tau = z^\dagger z = 0$, which consequently reduces Eq. (A9) to the form presented in Eq. (6). Second, although Ref. [74] showed that using a Lagrange multiplier method to enforce both energy and trace preservation does not, in general, result in the unitary evolution expected for an isolated system; any linear parametrization as the one in Eq. (4) is exempt from this problem.

APPENDIX B: COMPUTATIONAL DETAILS

The integration of the evolution problem presented in Eq. (6) relies exclusively on linear algebra operations involving matrices of dimensions $N_{\mathcal{H}} \times M$ (z and $\tilde{\mathbf{L}}$) and/or $M \times M$ (\mathbf{S} , \mathbf{L} , and \mathbf{B}), where $M \ll N$. This disparity in dimensions allows for efficient execution of these operations, given the relatively smaller size of at least one dimension of each matrix. The bulk of the computational effort is dedicated to calculating the matrix $\tilde{\mathbf{L}}$, defined as:

$$\begin{aligned}
\tilde{\mathbf{L}} &= \mathcal{L}(\rho)z = \left[-i(\hat{H}_{\text{eff}}\hat{\rho} - \hat{\rho}\hat{H}_{\text{eff}}^\dagger) + \sum_{\sigma=1}^D \hat{\Gamma}_\sigma \hat{\rho} \hat{\Gamma}_\sigma^\dagger \right] z \\
&= -i(\hat{H}_{\text{eff}}z\mathbf{B})\mathbf{S} + iz[(\hat{H}_{\text{eff}}z\mathbf{B})^\dagger z] + \sum_{\sigma=1}^D (\hat{\Gamma}_\sigma z)\mathbf{B}[(\hat{\Gamma}_\sigma z)^\dagger z].
\end{aligned} \tag{B1}$$

By following the order of operations as indicated by the parentheses in the equation, the computation of $\tilde{\mathbf{L}}$ involves matrix-matrix multiplications between $M \times M$ matrices, $N_{\mathcal{H}} \times M$ and $M \times M$ matrices, as well as between extremely sparse $N_{\mathcal{H}} \times N_{\mathcal{H}}$ and dense $N_{\mathcal{H}} \times M$ matrices. This approach ensures that no dense $N_{\mathcal{H}} \times N_{\mathcal{H}}$ matrix is ever stored in memory or involved in any multiplication. The process is optimized for efficiency, leveraging the reduced dimensionality to minimize the computational load, and free from the diagonalization of large matrices required in Refs. [68–70].

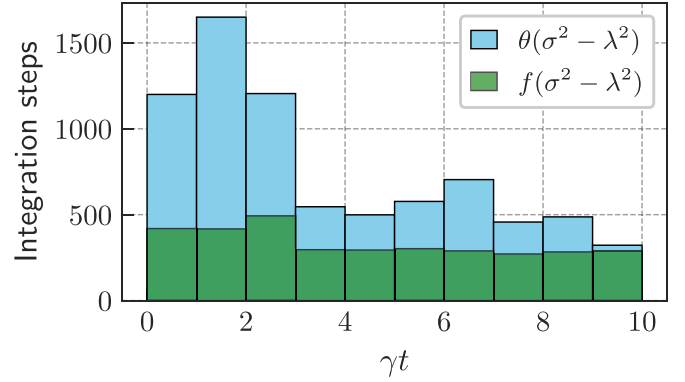


FIG. 11. Number of integration steps in of the adaptive integrator as a function of time. We simulate the evolution of the XYZ model with $N = 9$ spins and $J_y = 1$. The remaining physical parameters are set to the values discussed in Sec. III A. We evolve while dynamically adjusting the rank with a threshold of $\epsilon_{\text{max}} = 10^{-4}$. The regularization parameters are $\text{atol} = 10^{-6}$ and $\text{rtol} = 10^{-5}$.

The integration of Eq. (6) does, however, necessitate the calculation of the inverse matrices of \mathbf{S} and \mathbf{B} . Since these matrices may be singular, their inverse is often ill defined. In order to progress, regularization schemes are typically employed. A common approach involves adding a small diagonal contribution to the matrices to mitigate the impact of small eigenvalues. Yet, we have found that the effect of such an addition is not well controlled during time evolution, particularly when using an adaptive integrator. Similar observations were reported in Ref. [83]. Taking inspiration from this work, we adopt a regularization scheme based on the singular value decomposition of $\mathbf{S} = \mathbf{U}\mathbf{\Sigma}\mathbf{V}^\dagger$, where $\mathbf{\Sigma} = \text{diag}(\sigma_1^2, \dots, \sigma_M^2)$. Specifically, we define the pseudoinverse of \mathbf{S} as $\mathbf{S}^{-1} = \mathbf{V}\mathbf{\Sigma}^+\mathbf{U}^\dagger$, where

$$\Sigma_{\mu\nu}^+ = \frac{f(\sigma_\mu^2)}{\sigma_\mu^2} \delta_{\mu\nu} \quad \text{with} \quad f(\sigma^2) = \frac{1}{1 + \left(\frac{\lambda^2}{\sigma^2}\right)^6}. \tag{B2}$$

We do the same for \mathbf{B} . The value of λ is chosen adaptively at each iteration according to

$$\lambda^2 = \lambda^2(\sigma_1^2, \dots, \sigma_M^2) = \max \left[\text{atol}, \text{rtol} \times \max_{\mu} (\sigma_\mu^2) \right]. \tag{B3}$$

Throughout the paper we set $\text{atol} = 10^{-6}$. Note that the Moore-Penrose pseudoinverse corresponds to choosing the discontinuous function $f(\sigma^2) = \theta(\sigma^2 - \lambda^2)$. In line with the results from Ref. [83], we find that opting for a smooth functional form for $f(\sigma^2)$ significantly enhances the stability and efficiency of the adaptive time stepping in the integration routine. This improvement is illustrated in Fig. 11, where we plot the number of integration steps required as a function of time.

APPENDIX C: THE LOW-RANK DYNAMICAL TRUNCATION SCHEME

We review here the ensemble truncation methods (or *low-rank dynamical truncation schemes*) introduced in Refs. [68–70]. The starting assumption is that, at time t , the

system is described by a LR density matrix in diagonal form,

$$\hat{\rho}(t) = \sum_{j=1}^{M(t)} p_j |\varphi_j\rangle\langle\varphi_j|, \quad (\text{C1})$$

where $\langle\varphi_j|\varphi_k\rangle = \delta_{jk}$ and $M(t) \equiv M$ for notational clarity. The evolved state $\hat{\rho}(t + dt)$ can be written in terms of the Kraus operators as

$$\hat{\rho}(t + dt) = \sum_{j=0}^D \hat{K}_j \hat{\rho}(t) \hat{K}_j^\dagger + \mathcal{O}dt^2, \quad (\text{C2})$$

where

$$\hat{K}_0 = \mathbb{1} - i\hat{H}_{\text{eff}}dt, \quad \hat{H}_{\text{eff}} = \hat{H} - \frac{i}{2} \sum_{\sigma=1}^D \hat{\Gamma}_\sigma^\dagger \hat{\Gamma}_\sigma, \quad (\text{C3})$$

and

$$\hat{K}_\sigma = \hat{\Gamma}_\sigma \sqrt{dt} \quad \text{for } \sigma = 1, \dots, D. \quad (\text{C4})$$

Both $\hat{\rho}(t) = \mathbf{C}\mathbf{C}^\dagger$ and $\hat{\rho}(t + dt) = \mathbf{T}\mathbf{T}^\dagger$ are then conveniently rewritten in terms of

$$\begin{aligned} \mathbf{C} &= [\sqrt{p_j} z_{\alpha j}] & \text{with } \dim(\mathbf{C}) &= N_{\mathcal{H}} \times M, \\ \mathbf{T} &= [\langle e_\alpha | \hat{K}_\sigma | \varphi_k \rangle] & \text{with } \dim(\mathbf{T}) &= N_{\mathcal{H}} \times M(D + 1), \end{aligned} \quad (\text{C5})$$

where $\sigma = 0, \dots, D, k = 1, \dots, M$, and $l = M\sigma + k$.

The dynamical truncation scheme consists, at each time step, in (i) computing the matrix \mathbf{T} , (ii) diagonalizing $\hat{\rho}(t + dt)$, and (iii) truncating the subspace by retaining only the eigenstates with the largest eigenvalues \tilde{p}_j . This last step determines the new rank $M(t + dt)$, according to the criterion,

$$\epsilon_{M(t+dt)} \equiv \left[1 - \sum_{j=1}^{M(t+dt)} \tilde{p}_j \right] \leq \epsilon_{\text{max}} \ll 1, \quad (\text{C6})$$

where ϵ_{max} is the upper bound discussed in Sec. II B. The new truncated density matrix reads

$$\hat{\rho}(t + dt) = \sum_{j=1}^{M(t+dt)} \tilde{p}_j |\tilde{\varphi}_j\rangle\langle\tilde{\varphi}_j|, \quad (\text{C7})$$

with $|\tilde{\varphi}_j\rangle$ the first $M(t + dt)$ eigenvectors of $\mathbf{T}\mathbf{T}^\dagger$ with the largest eigenvalues. The apparent difficulty in diagonalizing the $N_{\mathcal{H}} \times N_{\mathcal{H}}$ density matrix $\mathbf{T}\mathbf{T}^\dagger$ is avoided by noticing that the $M \times M$ matrix $\mathbf{T}^\dagger\mathbf{T}$ has the same nonvanishing eigenvalues as its adjoint with the associated eigenvectors being linearly related through \mathbf{T} .

1. First-order equivalence of the two schemes

In this section we set out to prove the equivalence, to first order in perturbation theory, between the schemes in Refs. [68–70] and the present LR-TDVP method summarized by the EOM (6). To do so we make the following two assumptions. First, we assume that at time t the system density matrix

$\hat{\rho}(t)$ is in its diagonal spectral form (C1), that is,

$$\begin{aligned} \mathbf{B} &= \text{diag}(p_1, \dots, p_M), \\ \mathbf{B}^{-1} &= \text{diag}\left(\frac{1}{p_1}, \dots, \frac{1}{p_M}\right), \\ \mathbf{S} &= \mathbf{S}^{-1} = \mathbb{1}. \end{aligned} \quad (\text{C8})$$

Second, we assume the rank M of $\hat{\rho}(t)$ to be unchanged at time $t + dt$. Within these assumptions, the variational Eq. (6) can be cast in the compact form

$$\dot{\mathbf{B}} = \mathbf{L}, \quad (\text{C9})$$

$$|\dot{\varphi}_j\rangle = \frac{[\mathbb{1} - \mathbf{P}]\mathcal{L}(\hat{\rho})}{p_j} |\varphi_j\rangle. \quad (\text{C10})$$

Note that since the dynamical truncation scheme does not enforce trace preservation, in this section neither do we. Indeed, Eq. (C9) does not include the additional term $-\mathbb{1}\text{Tr}\{\mathbf{L}\}/M$ enforcing trace preservation in Eq. (6). The proof now consists in showing that the diagonal matrix (C7) produced by the dynamical truncation scheme coincides with that generated by Eqs. (C9) and (C10) to leading order in dt . To complete the proof, we express the density operator $\hat{\rho}(t + dt)$ to leading order in dt as

$$\begin{aligned} \hat{\rho}(t + dt) &= \sum_{j=1}^M p_j |\varphi_j\rangle\langle\varphi_j| + \mathcal{L}[\hat{\rho}(t)]dt \\ &= \sum_{j=1}^M p_j |\varphi_j\rangle\langle\varphi_j| + \sum_{j,k=1}^{N_{\mathcal{H}}} \mathbf{L}_{jk} |\varphi_j\rangle\langle\varphi_k| dt, \end{aligned} \quad (\text{C11})$$

where we have completed the orthogonal basis of the full Hilbert space by introducing a set of orthogonal vectors $\{|\varphi_j\rangle, j = M + 1, \dots, N_{\mathcal{H}}\}$. The dynamical truncation scheme is achieved by diagonalizing the matrix $\hat{\rho}(t + dt)$ in Eq. (C11). The first term in Eq. (C11) is diagonal in the LR subspace \mathcal{H}_M and thus has nonzero diagonal elements p_j for $j = 1, \dots, M$ only. The second term is nondiagonal and small. The eigenvalue perturbation theory, therefore, achieves the diagonalization to leading order in dt . According to perturbation theory, the new eigenvalues and eigenvectors are expressed as

$$\tilde{p}_j = p_j + \mathbf{L}_{jj}dt, \quad (\text{C12})$$

$$|\tilde{\varphi}_j\rangle = |\varphi_j\rangle + \sum_{k \neq j}^{1,M} |\varphi_k\rangle \frac{\mathbf{L}_{kj}}{p_j - p_k} dt \quad (\text{C13})$$

$$+ \left(\sum_{k=M+1}^N |\varphi_k\rangle\langle\varphi_k| \right) \frac{\mathcal{L}(\hat{\rho})|\varphi_j\rangle}{p_j} dt, \quad (\text{C14})$$

where we have distinguished the terms with $j = 1, \dots, M$ from the other terms in the sum over states orthogonal to the LR subspace. Notice that in the last term of Eq. (C13) the sum over the projectors $|\varphi_k\rangle\langle\varphi_k|$ factors out, as in the unperturbed matrix $p_k = 0$ for $k > M$. Using that

$\mathbb{1} - \mathbf{P} = \sum_{k=M+1}^{N_{\mathcal{H}}} |\varphi_k\rangle\langle\varphi_k|$, we immediately identify Eq. (C10) with the last term on the right-hand side of Eq. (C13). The remaining terms in Eq. (C13), together with Eq. (C12), are the perturbation-theory expansion of the $M \times M$ matrix in Eq. (C11). This concludes the proof.

The relation between the truncation error ϵ_M in Eq. (C6) and the approximated variational error in Eq. (10) is also made

clear from the first-order perturbative expansion. Indeed, if $\sum_j p_j = 1$, then

$$\epsilon_M = 1 - \sum_j \tilde{p}_j = -\text{Tr}\{\mathbf{L}\}dt \propto \text{Tr}\{\mathbf{P}\mathcal{L}(\hat{\rho})\} = \chi, \quad (\text{C15})$$

where we made use of the fact that $S^{-1} = \mathbb{1}$ for an orthonormal basis.

-
- [1] M. Brink, J. M. Chow, J. Hertzberg, E. Magesan and S. Rosenblatt, *Proceedings of the IEEE International Electron Devices Meeting (IEDM '18)* (IEEE, Los Alamitos, CA, 2018), pp. 6.1.1–6.1.3.
- [2] W. Cai, Y. Ma, W. Wang, C.-L. Zou, and L. Sun, Bosonic quantum error correction codes in superconducting quantum circuits, *Fundam. Res.* **1**, 50 (2021).
- [3] E. T. Campbell, B. M. Terhal, and C. Vuillot, Roads towards fault-tolerant universal quantum computation, *Nature (London)* **549**, 172 (2017).
- [4] A. Joshi, K. Noh, and Y. Y. Gao, Quantum information processing with bosonic qubits in circuit QED, *Quant. Sci. Technol.* **6**, 033001 (2021).
- [5] J. Kempe, D. Bacon, D. A. Lidar, and K. B. Whaley, Theory of decoherence-free fault-tolerant universal quantum computation, *Phys. Rev. A* **63**, 042307 (2001).
- [6] J. Preskill, Quantum computing in the NISQ era and beyond, *Quantum* **2**, 79 (2018).
- [7] B. M. Terhal, Quantum error correction for quantum memories, *Rev. Mod. Phys.* **87**, 307 (2015).
- [8] B. M. Terhal, J. Conrad, and C. Vuillot, Towards scalable bosonic quantum error correction, *Quant. Sci. Technol.* **5**, 043001 (2020).
- [9] F. Verstraete, M. M. Wolf, and J. I. Cirac, Quantum computation and quantum-state engineering driven by dissipation, *Nat. Phys.* **5**, 633 (2009).
- [10] A. Polkovnikov, K. Sengupta, A. Silva, and M. Vengalattore, Colloquium: Nonequilibrium dynamics of closed interacting quantum systems, *Rev. Mod. Phys.* **83**, 863 (2011).
- [11] J. Eisert, M. Friesdorf, and C. Gogolin, Quantum many-body systems out of equilibrium, *Nat. Phys.* **11**, 124 (2015).
- [12] R. Blume-Kohout, H. K. Ng, D. Poulin, and L. Viola, Information-preserving structures: A general framework for quantum zero-error information, *Phys. Rev. A* **82**, 062306 (2010).
- [13] E. Knill, R. Laflamme, and L. Viola, Theory of quantum error correction for general noise, *Phys. Rev. Lett.* **84**, 2525 (2000).
- [14] D. A. Lidar and T. A. Brun, *Quantum Error Correction* (Cambridge University Press, Cambridge, UK, 2013).
- [15] D. A. Lidar, *Quantum Information and Computation for Chemistry* (Wiley, New York, 2014), pp. 295–354.
- [16] L. Gravina, F. Minganti, and V. Savona, Critical Schrödinger Cat Qubit, *PRX Quant.* **4**, 020337 (2023).
- [17] Y.-J. Liu and S. Lieu, Dissipative phase transitions and passive error correction, *Phys. Rev. A* **109**, 022422 (2024).
- [18] S. Lieu, R. Belyansky, J. T. Young, R. Lundgren, V. V. Albert, and A. V. Gorshkov, Symmetry breaking and error correction in open quantum systems, *Phys. Rev. Lett.* **125**, 240405 (2020).
- [19] Z. Leghtas, S. Touzard, I. M. Pop, A. Kou, B. Vlastakis, A. Petrenko, K. M. Sliwa, A. Narla, S. Shankar, M. J. Hatridge, M. Reagor, L. Frunzio, R. J. Schoelkopf, M. Mirrahimi, and M. H. Devoret, Confining the state of light to a quantum manifold by engineered two-photon loss, *Science* **347**, 853 (2015).
- [20] S. Touzard, A. Grimm, Z. Leghtas, S. O. Mundhada, P. Reinhold, C. Axline, M. Reagor, K. Chou, J. Blumoff, K. M. Sliwa, S. Shankar, L. Frunzio, R. J. Schoelkopf, M. Mirrahimi, and M. H. Devoret, Coherent oscillations inside a quantum manifold stabilized by dissipation, *Phys. Rev. X* **8**, 021005 (2018).
- [21] R. Di Candia, F. Minganti, K. V. Petrovnin, G. S. Paraoanu, and S. Felicetti, Critical parametric quantum sensing, *npj Quant. Inf.* **9**, 23 (2023).
- [22] S. Fernández-Lorenzo and D. Porras, Quantum sensing close to a dissipative phase transition: Symmetry breaking and criticality as metrological resources, *Phys. Rev. A* **96**, 013817 (2017).
- [23] T. Ilias, D. Yang, S. F. Huelga, and M. B. Plenio, Criticality-enhanced quantum sensing via continuous measurement, *PRX Quant.* **3**, 010354 (2022).
- [24] Z. Gong, Y. Ashida, K. Kawabata, K. Takasan, S. Higashikawa, and M. Ueda, Topological phases of non-Hermitian systems, *Phys. Rev. X* **8**, 031079 (2018).
- [25] K. Kawabata, K. Shiozaki, M. Ueda, and M. Sato, Symmetry and topology in non-Hermitian physics, *Phys. Rev. X* **9**, 041015 (2019).
- [26] R. Hamazaki, K. Kawabata, and M. Ueda, Non-Hermitian many-body localization, *Phys. Rev. Lett.* **123**, 090603 (2019).
- [27] M. Ippoliti, M. J. Gullans, S. Gopalakrishnan, D. A. Huse, and V. Khemani, Entanglement phase transitions in measurement-only dynamics, *Phys. Rev. X* **11**, 011030 (2021).
- [28] K. Kawabata, T. Numasawa, and S. Ryu, Entanglement phase transition induced by the non-Hermitian skin effect, *Phys. Rev. X* **13**, 021007 (2023).
- [29] I. M. Georgescu, S. Ashhab, and F. Nori, Quantum simulation, *Rev. Mod. Phys.* **86**, 153 (2014).
- [30] V. Gorini, A. Frigerio, M. Verri, A. Kossakowski, and E. C. G. Sudarshan, Properties of quantum Markovian master equations, *Rep. Math. Phys.* **13**, 149 (1978).
- [31] G. Lindblad, On the generators of quantum dynamical semigroups, *Commun. Math. Phys.* **48**, 119 (1976).
- [32] V. Gorini, A. Kossakowski, and E. C. G. Sudarshan, Completely positive dynamical semigroups of N -level systems, *J. Math. Phys.* **17**, 821 (1976).
- [33] I. Rotter and J. P. Bird, A review of progress in the physics of open quantum systems: Theory and experiment, *Rep. Prog. Phys.* **78**, 114001 (2015).

- [34] H. Weimer, A. Kshetrimayum, and R. Orús, Simulation methods for open quantum many-body systems, *Rev. Mod. Phys.* **93**, 015008 (2021).
- [35] A. J. Daley, Quantum trajectories and open many-body quantum systems, *Adv. Phys.* **63**, 77 (2014).
- [36] W. Verstraelen, D. Huybrechts, T. Roscilde, and M. Wouters, Quantum and classical correlations in open quantum spin lattices via truncated-cumulant trajectories, *PRX Quant.* **4**, 030304 (2023).
- [37] A. Polkovnikov, Phase space representation of quantum dynamics, *Ann. Phys.* **325**, 1790 (2010).
- [38] P. Deuar, A. Ferrier, M. Matuszewski, G. Orso, and M. H. Szymańska, Fully quantum scalable description of driven-dissipative lattice models, *PRX Quant.* **2**, 010319 (2021).
- [39] J. Jin, A. Biella, O. Viyuela, L. Mazza, J. Keeling, R. Fazio, and D. Rossini, Cluster mean-field approach to the steady-state phase diagram of dissipative spin systems, *Phys. Rev. X* **6**, 031011 (2016).
- [40] D. Huybrechts, F. Minganti, F. Nori, M. Wouters, and N. Shammah, Validity of mean-field theory in a dissipative critical system: Liouvillian gap, $\mathbb{P}\mathbb{T}$ -symmetric antigap, and permutational symmetry in the XYZ model, *Phys. Rev. B* **101**, 214302 (2020).
- [41] U. Schollwöck, The density-matrix renormalization group, *Rev. Mod. Phys.* **77**, 259 (2005).
- [42] U. Schollwöck, The density-matrix renormalization group in the age of matrix product states, *Ann. Phys.* **326**, 96 (2011).
- [43] S. Paeckel, T. Köhler, A. Swoboda, S. R. Manmana, U. Schollwöck, and C. Hubig, Time-evolution methods for matrix-product states, *Ann. Phys.* **411**, 167998 (2019).
- [44] J. Eisert, Entanglement and tensor network states, *Model. Simul.* **3**, 520 (2013).
- [45] N. Feldman, A. Kshetrimayum, J. Eisert, and M. Goldstein, Entanglement estimation in tensor network states via sampling, *PRX Quant.* **3**, 030312 (2022).
- [46] R. Orús, A practical introduction to tensor networks: Matrix product states and projected entangled pair states, *Ann. Phys.* **349**, 117 (2014).
- [47] J. I. Cirac, D. Pérez-García, N. Schuch, and F. Verstraete, Matrix product states and projected entangled pair states: Concepts, symmetries, theorems, *Rev. Mod. Phys.* **93**, 045003 (2021).
- [48] X. Yuan, S. Endo, Q. Zhao, Y. Li, and S. C. Benjamin, Theory of variational quantum simulation, *Quantum* **3**, 191 (2019).
- [49] S. Endo, J. Sun, Y. Li, S. C. Benjamin, and X. Yuan, Variational quantum simulation of general processes, *Phys. Rev. Lett.* **125**, 010501 (2020).
- [50] M. Reh, M. Schmitt, and M. Gärtner, Time-dependent variational principle for open quantum systems with artificial neural networks, *Phys. Rev. Lett.* **127**, 230501 (2021).
- [51] F. Azad, A. Hallam, J. Morley, and A. G. Green, Phase transitions in the classical simulability of open quantum systems, *Sci. Rep.* **13**, 8866 (2023).
- [52] Y. Wu, Time-dependent variational principle for mixed matrix product states in the thermodynamic limit, *Phys. Rev. B* **102**, 134306 (2020).
- [53] T. Gerds and U. Manthe, A wave packet approach to the Liouville–von Neumann equation for dissipative systems, *J. Chem. Phys.* **106**, 3017 (1997).
- [54] A. Raab, I. Burghardt, and H.-D. Meyer, The multiconfiguration time-dependent Hartree method generalized to the propagation of density operators, *J. Chem. Phys.* **111**, 8759 (1999).
- [55] I. Burghardt, H.-D. Meyer, and L. S. Cederbaum, Approaches to the approximate treatment of complex molecular systems by the multiconfiguration time-dependent Hartree method, *J. Chem. Phys.* **111**, 2927 (1999).
- [56] M. J. Hartmann and G. Carleo, Neural-network approach to dissipative quantum many-body dynamics, *Phys. Rev. Lett.* **122**, 250502 (2019).
- [57] A. Nagy and V. Savona, Variational quantum Monte Carlo method with a neural-network ansatz for open quantum systems, *Phys. Rev. Lett.* **122**, 250501 (2019).
- [58] D. Luo, Z. Chen, J. Carrasquilla, and B. K. Clark, Autoregressive neural network for simulating open quantum systems via a probabilistic formulation, *Phys. Rev. Lett.* **128**, 090501 (2022).
- [59] J. Carrasquilla, G. Torlai, R. G. Melko, and L. Aolita, Reconstructing quantum states with generative models, *Nat. Mach. Intell.* **1**, 155 (2019).
- [60] N. Yoshioka and R. Hamazaki, Constructing neural stationary states for open quantum many-body systems, *Phys. Rev. B* **99**, 214306 (2019).
- [61] F. Vicentini, A. Biella, N. Regnault, and C. Ciuti, Variational neural-network ansatz for steady states in open quantum systems, *Phys. Rev. Lett.* **122**, 250503 (2019).
- [62] A. Nagy and V. Savona, Driven-dissipative quantum Monte Carlo method for open quantum systems, *Phys. Rev. A* **97**, 052129 (2018).
- [63] C. Pagliantini and F. Vismara, Fully adaptive structure-preserving hyper-reduction of parametric Hamiltonian systems, [arXiv:2308.16547](https://arxiv.org/abs/2308.16547).
- [64] J. S. Hesthaven, C. Pagliantini and N. Ripamonti, Rank-adaptive structure-preserving model order reduction of Hamiltonian systems, [arXiv:2007.13153](https://arxiv.org/abs/2007.13153).
- [65] C. Pagliantini, Dynamical reduced basis methods for Hamiltonian systems, *Numer. Math.* **148**, 409 (2021).
- [66] N. Ezzell, Z. Holmes and P. J. Coles, The quantum low-rank approximation problem, [arXiv:2203.00811](https://arxiv.org/abs/2203.00811).
- [67] N. Ezzell, E. M. Ball, A. U. Siddiqui, M. M. Wilde, A. T. Sornborger, P. J. Coles, and Z. Holmes, Quantum mixed state compiling, *Quant. Sci. Technol.* **8**, 035001 (2023).
- [68] K. Donatella, Z. Denis, A. Le Boité, and C. Ciuti, Continuous-time dynamics and error scaling of noisy highly entangling quantum circuits, *Phys. Rev. A* **104**, 062407 (2021).
- [69] Y.-T. Chen, C. Farquhar, and R. M. Parrish, Low-rank density-matrix evolution for noisy quantum circuits, *npj Quant. Inf.* **7**, 61 (2021).
- [70] G. McCaul, K. Jacobs, and D. I. Bondar, Fast computation of dissipative quantum systems with ensemble rank truncation, *Phys. Rev. Res.* **3**, 013017 (2021).
- [71] C. Le Bris and P. Rouchon, Low-rank numerical approximations for high-dimensional Lindblad equations, *Phys. Rev. A* **87**, 022125 (2013).
- [72] H. Weimer, Variational principle for steady states of dissipative quantum many-body systems, *Phys. Rev. Lett.* **114**, 040402 (2015).

- [73] L. Joubert-Doriol, I. G. Ryabinkin, and A. F. Izmaylov, Non-stochastic matrix Schrödinger equation for open systems, *J. Chem. Phys.* **141**, 234112 (2014).
- [74] L. Joubert-Doriol and A. F. Izmaylov, Problem-free time-dependent variational principle for open quantum systems, *J. Chem. Phys.* **142**, 134107 (2015).
- [75] F. Verstraete, J. J. García-Ripoll, and J. I. Cirac, Matrix product density operators: Simulation of finite-temperature and dissipative systems, *Phys. Rev. Lett.* **93**, 207204 (2004).
- [76] M. Zwolak and G. Vidal, Mixed-state dynamics in one-dimensional quantum lattice systems: A time-dependent superoperator renormalization algorithm, *Phys. Rev. Lett.* **93**, 207205 (2004).
- [77] J. Cui, J. I. Cirac, and M. C. Bañuls, Variational matrix product operators for the steady state of dissipative quantum systems, *Phys. Rev. Lett.* **114**, 220601 (2015).
- [78] E. Mascarenhas, H. Flayac, and V. Savona, Matrix-product-operator approach to the nonequilibrium steady state of driven-dissipative quantum arrays, *Phys. Rev. A* **92**, 022116 (2015).
- [79] A. H. Werner, D. Jaschke, P. Silvi, M. Kliesch, T. Calarco, J. Eisert, and S. Montangero, Positive tensor network approach for simulating open quantum many-body systems, *Phys. Rev. Lett.* **116**, 237201 (2016).
- [80] A. Mercurio, L. Gravina, and Y.-T. Huang, QuantumToolbox.jl, <https://zenodo.org/records/10950251>.
- [81] J. Bezanson, A. Edelman, S. Karpinski, and V. B. Shah, Julia: A fresh approach to numerical computing, *SIAM Rev.* **59**, 65 (2017).
- [82] L. Gravina, Igravina1997/LowRankDynamics, <https://zenodo.org/records/10868390>.
- [83] M. Medvidović and D. Sels, Variational quantum dynamics of two-dimensional rotor models, *PRX Quant.* **4**, 040302 (2023).
- [84] J. Loreaux and G. Weiss, Majorization and a Schur–Horn theorem for positive compact operators, the nonzero kernel case, *J. Funct. Anal.* **268**, 703 (2015).
- [85] A. Raab and H.-D. Meyer, Multiconfigurational expansions of density operators: equations of motion and their properties, *Theor. Chem. Acc.* **104**, 358 (2000).
- [86] G. Beaulieu, F. Minganti, S. Frasca, V. Savona, S. Felicetti, R. Di Candia and P. Scarlino, Observation of first- and second-order dissipative phase transitions in a two-photon driven Kerr resonator, [arXiv:2310.13636](https://arxiv.org/abs/2310.13636).
- [87] F. Minganti, I. I. Arkhipov, A. Miranowicz and F. Nori, Liouvillian spectral collapse in the Scully-Lamb laser model, *Phys. Rev. Res.* **3**, 043197 (2021).
- [88] F. Minganti, I. I. Arkhipov, A. Miranowicz, and F. Nori, Continuous dissipative phase transitions with or without symmetry breaking, *New J. Phys.* **23**, 122001 (2021).
- [89] F. Minganti, V. Savona, and A. Biella, Dissipative phase transitions in n -photon driven quantum nonlinear resonators, *Quantum* **7**, 1170 (2023).
- [90] F. Minganti, N. Bartolo, J. Lolli, W. Casteels, and C. Ciuti, Exact results for Schrödinger cats in driven-dissipative systems and their feedback control, *Sci. Rep.* **6**, 26987 (2016).
- [91] F. Minganti, Out-of-equilibrium phase transitions in nonlinear optical systems, Ph.D. thesis, Université Sorbonne Paris Cité, 2018.
- [92] F. Minganti, A. Biella, N. Bartolo, and C. Ciuti, Spectral theory of Liouvillians for dissipative phase transitions, *Phys. Rev. A* **98**, 042118 (2018).
- [93] N. Bartolo, F. Minganti, W. Casteels, and C. Ciuti, Exact steady state of a Kerr resonator with one- and two-photon driving and dissipation: Controllable Wigner-function multimodality and dissipative phase transitions, *Phys. Rev. A* **94**, 033841 (2016).
- [94] H. J. Carmichael, Breakdown of photon blockade: A dissipative quantum phase transition in zero dimensions, *Phys. Rev. X* **5**, 031028 (2015).
- [95] E. M. Kessler, G. Giedke, A. Imamoglu, S. F. Yelin, M. D. Lukin, and J. I. Cirac, Dissipative phase transition in a central spin system, *Phys. Rev. A* **86**, 012116 (2012).
- [96] T. E. Lee, S. Gopalakrishnan, and M. D. Lukin, Unconventional magnetism via optical pumping of interacting spin systems, *Phys. Rev. Lett.* **110**, 257204 (2013).
- [97] J. Benary, C. Baals, E. Bernhart, J. Jiang, M. Röhrle, and H. Ott, Experimental observation of a dissipative phase transition in a multi-mode many-body quantum system, *New J. Phys.* **24**, 103034 (2022).
- [98] L. M. Sieberer, S. D. Huber, E. Altman, and S. Diehl, Dynamical critical phenomena in driven-dissipative systems, *Phys. Rev. Lett.* **110**, 195301 (2013).
- [99] V. Savona, Spontaneous symmetry breaking in a quadratically driven nonlinear photonic lattice, *Phys. Rev. A* **96**, 033826 (2017).
- [100] R. Rota, F. Storme, N. Bartolo, R. Fazio, and C. Ciuti, Critical behavior of dissipative two-dimensional spin lattices, *Phys. Rev. B* **95**, 134431 (2017).
- [101] W. Casteels, R. M. Wilson, and M. Wouters, Gutzwiller Monte Carlo approach for a critical dissipative spin model, *Phys. Rev. A* **97**, 062107 (2018).
- [102] D. Rossini and E. Vicari, Coherent and dissipative dynamics at quantum phase transitions, *Phys. Rep.* **936**, 1 (2021).
- [103] X. Li, Y. Li, and J. Jin, Steady-state susceptibility in continuous phase transitions of dissipative systems, *Phys. Rev. A* **105**, 052226 (2022).
- [104] G. H. Wannier, Antiferromagnetism: The triangular Ising net, *Phys. Rev.* **79**, 357 (1950).
- [105] R. Rota and V. Savona, Simulating frustrated antiferromagnets with quadratically driven QED cavities, *Phys. Rev. A* **100**, 013838 (2019).
- [106] R. Rota, F. Minganti, C. Ciuti, and V. Savona, Quantum critical regime in a quadratically driven nonlinear photonic lattice, *Phys. Rev. Lett.* **122**, 110405 (2019).
- [107] C. Gerry and P. Knight, *Introductory Quantum Optics* (Cambridge University Press, Cambridge, UK, 2004).
- [108] D. Gottesman, A. Kitaev, and J. Preskill, Encoding a qubit in an oscillator, *Phys. Rev. A* **64**, 012310 (2001).
- [109] P. T. Cochrane, G. J. Milburn, and W. J. Munro, Macroscopically distinct quantum-superposition states as a bosonic code for amplitude damping, *Phys. Rev. A* **59**, 2631 (1999).
- [110] H. Goto, Universal quantum computation with a nonlinear oscillator network, *Phys. Rev. A* **93**, 050301(R) (2016).
- [111] M. Mirrahimi, Z. Leghtas, V. V. Albert, S. Touzard, R. J. Schoelkopf, L. Jiang, and M. H. Devoret, Dynamically protected cat-qubits: A new paradigm for universal quantum computation, *New J. Phys.* **16**, 045014 (2014).
- [112] J. Guillaud and M. Mirrahimi, Repetition cat qubits for fault-tolerant quantum computation, *Phys. Rev. X* **9**, 041053 (2019).
- [113] V. V. Albert, B. Bradlyn, M. Fraas, and L. Jiang, Geometry and response of Lindbladians, *Phys. Rev. X* **6**, 041031 (2016).

- [114] V. V. Albert, K. Noh, K. Duivenvoorden, D. J. Young, R. T. Brierley, P. Reinhold, C. Vuillot, L. Li, C. Shen, S. M. Girvin, B. M. Terhal, and L. Jiang, Performance and structure of single-mode bosonic codes, *Phys. Rev. A* **97**, 032346 (2018).
- [115] J. Guillaud, J. Cohen, and M. Mirrahimi, Quantum computation with cat qubits, *SciPost Phys. Lect. Not.* **72** (2023).
- [116] L. Gilles, B. M. Garraway, and P. L. Knight, Generation of nonclassical light by dissipative two-photon processes, *Phys. Rev. A* **49**, 2785 (1994).
- [117] E. E. Hach III and C. C. Gerry, Generation of mixtures of Schrödinger-cat states from a competitive two-photon process, *Phys. Rev. A* **49**, 490 (1994).
- [118] S. Puri, S. Boutin, and A. Blais, Engineering the quantum states of light in a Kerr-nonlinear resonator by two-photon driving, *npj Quant. Inf.* **3**, 18 (2017).
- [119] S. Puri, A. Grimm, P. Campagne-Ibarcq, A. Eickbusch, K. Noh, G. Roberts, L. Jiang, M. Mirrahimi, M. H. Devoret, and S. M. Girvin, Stabilized cat in a driven nonlinear cavity: A fault-tolerant error syndrome detector, *Phys. Rev. X* **9**, 041009 (2019).
- [120] S. Puri, L. St-Jean, J. A. Gross, A. Grimm, N. E. Frattini, P. S. Iyer, A. Krishna, S. Touzard, L. Jiang, A. Blais, S. T. Flammia, and S. M. Girvin, Bias-preserving gates with stabilized cat qubits, *Sci. Adv.* **6**, eaay5901 (2020).
- [121] A. Grimm, N. E. Frattini, S. Puri, S. O. Mundhada, S. Touzard, M. Mirrahimi, S. M. Girvin, S. Shankar, and M. H. Devoret, Stabilization and operation of a Kerr-cat qubit, *Nature (London)* **584**, 205 (2020).
- [122] J. Venkatraman, R. G. Cortinas, N. E. Frattini, X. Xiao, and M. H. Devoret, Quantum interference of tunneling paths under a double-well barrier, [arXiv:2211.04605](https://arxiv.org/abs/2211.04605).
- [123] C. Chamberland, K. Noh, P. Arrangoiz-Arriola, E. T. Campbell, C. T. Hann, J. Iverson, H. Putterman, T. C. Bohdanowicz, S. T. Flammia, A. Keller, G. Refael, J. Preskill, L. Jiang, A. H. Safavi-Naeini, O. Painter, and F. G. Brandão, Building a fault-tolerant quantum computer using concatenated cat codes, *PRX Quant.* **3**, 010329 (2022).
- [124] R. Gautier, A. Sarlette, and M. Mirrahimi, Combined dissipative and Hamiltonian confinement of cat qubits, *PRX Quant.* **3**, 020339 (2022).
- [125] J. Guillaud and M. Mirrahimi, Error rates and resource overheads of repetition cat qubits, *Phys. Rev. A* **103**, 042413 (2021).
- [126] J. Chávez-Carlos, T. L. M. Lezama, R. G. Cortiñas, J. Venkatraman, M. H. Devoret, V. S. Batista, F. Pérez-Bernal, and L. F. Santos, Spectral kissing and its dynamical consequences in the squeeze-driven Kerr oscillator, *npj Quantum Info.* **9**, 76 (2023).
- [127] S. Haroche and J.-M. Raimond, *Exploring the Quantum: Atoms, Cavities, and Photons* (Oxford University Press, Oxford, 2013).
- [128] Q. Xu, J. K. Iverson, F. G. S. L. Brandão, and L. Jiang, Engineering fast bias-preserving gates on stabilized cat qubits, *Phys. Rev. Res.* **4**, 013082 (2022).
- [129] V. V. Albert and L. Jiang, Symmetries and conserved quantities in Lindblad master equations, *Phys. Rev. A* **89**, 022118 (2014).
- [130] V. V. Albert, Lindbladians with multiple steady states: Theory and applications, [arXiv:1802.00010](https://arxiv.org/abs/1802.00010).
- [131] M. A. Nielsen and I. L. Chuang, *Quantum Computation and Quantum Information: 10th Anniversary Edition* (Cambridge University Press, New York, 2011).
- [132] F.-M. L. Régent and P. Rouchon, Adiabatic elimination for composite open quantum systems: Reduced model formulation and numerical simulations, [arXiv:2303.05089](https://arxiv.org/abs/2303.05089) [quant-ph].
- [133] R. Orús, Tensor networks for complex quantum systems, *Nat. Rev. Phys.* **1**, 538 (2019).
- [134] G. Carleo and M. Troyer, Solving the quantum many-body problem with artificial neural networks, *Science* **355**, 602 (2017).
- [135] I. de Vega and D. Alonso, Dynamics of non-Markovian open quantum systems, *Rev. Mod. Phys.* **89**, 015001 (2017).
- [136] H.-P. Breuer and F. Petruccione, *The Theory of Open Quantum Systems* (Oxford University Press, Oxford, 2007).
- [137] K. Temme, S. Bravyi, and J. M. Gambetta, Error mitigation for short-depth quantum circuits, *Phys. Rev. Lett.* **119**, 180509 (2017).
- [138] E. van den Berg, Z. K. Mineev, A. Kandala, and K. Temme, Probabilistic error cancellation with sparse Pauli-Lindblad models on noisy quantum processors, *Nat. Phys.* **19**, 1116 (2023).
- [139] Z. Cai, R. Babbush, S. C. Benjamin, S. Endo, W. J. Huggins, Y. Li, J. R. McClean, and T. E. O'Brien, Quantum error mitigation, *Rev. Mod. Phys.* **95**, 045005 (2023).